



Rigid–flexible–thermal coupling dynamics of a hub and multiplate system considering frictional contact

Tingting Yuan¹ · Bo Lei¹ · Jinyang Liu¹ · Yunli Wu²

Received: 2 December 2022 / Accepted: 30 June 2023 / Published online: 21 July 2023
© The Author(s), under exclusive licence to Springer Nature B.V. 2023

Abstract

A geometric nonlinear modeling approach for strong rigid–flexible–thermal coupling dynamics of a hub and multiplate system considering frictional contact is proposed. Based on the absolute nodal coordinate formulation (ANCF), an ANCF thin-plate element with thermoelasticity is developed, where the temperature field is expressed with Taylor polynomials to yield heat-conduction equations. In contrast to the traditional coupling formulations, the influences of the attitude motion and structural deformation on the intensity of the solar radiation, the geometric nonlinearity of the plate as well as the frictional contact are taken into account. The frictional-contact formulations for a thin plate and a rigid body are presented, which can capture the stick–slip transition and address the multiple-point contact scenarios. To solve the strong rigid–flexible–thermal coupling equations, a novel numerical approach combining the generalized- α method and the modified central-difference method is proposed. Two validations are performed to verify the proposed model, which proves the importance of considering the geometric nonlinearity and reveals the phenomena of thermally induced vibrations. Then, the thermal–dynamic coupling analysis for the satellite and solar-array multibody system in a thermal environment is carried out. The dynamic characteristics of the thermally induced vibration can be successfully revealed by the rigid–flexible–thermal coupling model. Furthermore, it is indicated that the influence of contact and thermal load on the nonlinear behavior of the solar-array deployment is essential, which demonstrates the feasibility of the proposed approach.

Keywords Geometric nonlinearity · Rigid–flexible–thermal coupling dynamics · Thermally induced vibration · Frictional contact

1 Introduction

Thermally induced vibrations of flexible spacecraft appendages may be initiated through the rapid changes of thermal loading during the orbital-eclipse transitions. The thermal gradient

✉ J. Liu
liujy@sjtu.edu.cn

¹ Department of Engineering Mechanics, Key Laboratory of Hydrodynamics (Ministry of Education), School of Naval Architecture, Ocean and Civil Engineering, Shanghai Jiao Tong University, Shanghai 200240, China

² Beijing Institute of Control Engineering & Key Laboratory of Space Intelligent Control Technology, Beijing 100190, China

in the thickness direction is caused by the difference of the heat flux applied on the upper and lower surfaces of the solar arrays, which may induce thermal deformation, thermal vibrations, and even influence the attitude motion of the satellite. Additionally, the thermal–dynamic modeling of the spacecraft in many cases involves contact interaction between flexible appendages undergoing large deformations and overall motions. Therefore, an accurate rigid–flexible–thermal coupling model is essential to guide the practical engineering applications, and this study remains a worthy and challenging area.

Concerning the investigation of the thermal–structural coupling effect, Thornton and Kim [1] developed an analytical approach for determining the dynamic response of a flexible rolled-up solar array due to a sudden increase in external heating, in which the rotational motion of the spacecraft was not taken into account. Johnston and Thornton [2] presented an analytical model to investigate the effects of thermally induced vibrations of the flexible appendages on the rotational motion of the spacecraft, and then further carried out an experimental investigation on the thermal–structural coupling dynamics [3]. Fan and Liu [4] developed a 2D rigid–flexible–thermal coupling model to investigate the thermally induced vibration of a hub–beam system. Shen et al. analyzed the thermal–structural coupling performance for a space thin-walled beam [5] and a spinning spacecraft with an axial boom [6], and further conducted a stability analysis for the thermally induced fluttering phenomena [7]. Čepon et al. [8] proposed a new model for a coupled thermal–structural analysis of the bimetallic strip based on the ANCF. Liu et al. [9–11] carried out a thermal–structural analysis for a flexible spacecraft with a single or double solar panels, in which the coupling effect among attitude motion, structural deformation, and thermal loading are taken into account. Li et al. [12] investigated rigid–flexible–thermal coupling dynamics for a hub–beam system with a clearance joint considering torsional spring, latch mechanism, and attitude controller.

Since the solar arrays are thin plates, it is necessary to extend the thermal–structural coupling investigation to plate structures. Liu et al. [13] investigated the dynamic performance of a hub–plate system. The influence of the rotational motion on the intensity of the heat flux was included in the dynamic model. However, the temperature field expressed by the 3D solid element is complicated, and the geometric nonlinearity as well as the contact between the flexible bodies were not considered.

The Absolute Nodal Coordinate Formulation (ANCF) proposed by Shabana [14] has been widely used for simulation of a plate with large deformation. Since the transverse shear deformable of a thin plate can be neglected, based on Kirchhoff assumptions, Dmitrochenko et al. [15, 16], Dufva [17], and Ren [18] parameterized the plate elements using slopes in the element midsurface direction only. Schwab et al. [19] and Sereshk and Mahmoud [20] compared the thin-plate elements against the plate element based on the conventional finite-element approach. Hyldahl et al. [21] also compared the convergence of rectangular thin-plate elements in different mesh configurations and load conditions. In ANCF, the gradient vectors are used to describe the nodal rotations instead of the rotation parameters, avoiding the singularity problem and the interpolation problem of the finite rotation variables [22–24]. Hence, ANCF is suitable for the geometric nonlinear dynamics modeling of rigid–flexible coupled or rigid–flexible–thermal coupled multibody systems. Based on an ANCF shear-deformable plate element, Shen et al. [25] proposed a coupled thermal–structural model of a laminated composite plate. Cui and Yu proposed a novel method of the thermomechanical coupled analysis based on the unified description [26], and further developed a thermal integrated ANCF thin plate, which depicts the displacement and the temperature field integratedly [27].

Since the contact may occur during the deployment of a hub and multiplate system, it is necessary to consider the effect of frictional contact in the rigid–flexible–thermal coupling modeling. The key to modeling the contact dynamics of multibody systems lies in the treatment of contact-interface nonlinearities, which involves contact detection, contact discretization, enforcement of contact conditions, and a friction-force model [28–31]. In recent years, some researchers have already developed several different formulations for modeling the frictional-contact problem in multibody systems. Konyukhov and Schweizerhof [32, 33] developed a geometrically exact theory for various 3D solid-contact elements, including the normal, the tangential, and the rotational interactions. Yu et al. [34] established the frictional-contact formulation between flexible and rigid bodies through the Hertz contact model and the velocity-based friction model. Shi et al. [35] presented a rotation-free shell formulation and an extended contact discretization for the dynamics of multibody systems with large deformations and frictionless contacts. Sun et al. [36, 37] developed a new 2D segment-to-segment algorithm of contact dynamics based on an ANCF and mortar method, including both frictionless and friction cases. Gay Neto et al. [38] proposed a formulation to handle pointwise frictional-contact interaction of a beam–shell system using the degeneration of the local-contact problem. Tang and Liu [39] modeled the frictional contact in sliding joints with clearances, and generalized the regularized Coulomb friction law into an ANCF beam and rigid hole considering the stick–slip transition. Lei et al. [40] presented a strong coupling modeling method for the rigid bodies and the large deformed beams in contact interaction with the granular matter to simulate the flexible-brush sampling process. To avoid mutual penetration of the plate element with large deformation, a mixed method combining the node-to-surface, edge-to-surface, and surface-to-surface contact elements based on ANCF was proposed by the authors [41, 42]. Nevertheless, few studies have considered the frictional contact interactions in the rigid–flexible–thermal coupling multibody systems.

In this paper, a strong rigid–flexible–thermal coupling dynamic model for a hub and multiplate system is proposed considering the geometric nonlinearity and frictional contact. The remainder of the paper is organized as follows. In Sect. 2, an ANCF thin-plate element with thermoelasticity is developed. Two frictional contact elements based on the ANCF thin-plate element are presented in Sect. 3. In Sect. 4, the heat-conduction equations with solar radiation are derived, and a complete rigid–flexible–thermal coupling model is introduced. In Sect. 5, a new numerical approach combining the generalized- α method and the modified central-difference method is proposed to solve the strong rigid–flexible–thermal coupling equations. Two validations are carried out to confirm the correctness of the proposed thermal–structural coupling model in Sect. 6. Section 7 presents two interesting engineering numerical simulations of the satellite and solar-array multibody system in a thermal environment. Summary and conclusions are presented in Sect. 8.

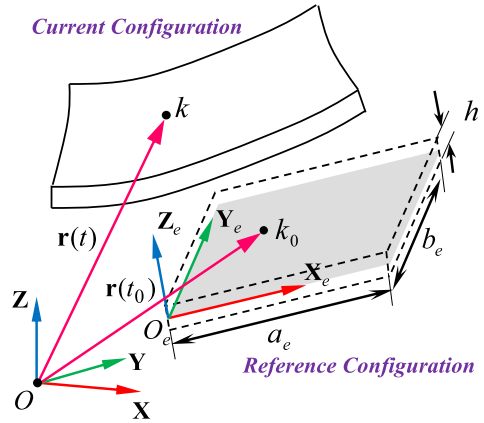
2 ANCF thin-plate element with thermoelasticity

A thin rectangular plate element with length a_e , width b_e , and height h , is shown in Fig. 1. As shown in the figure, $O\text{-}XYZ$ and $O_e\text{-}X_eY_eZ_e$ represent the inertial coordinate system and the element coordinate system, respectively.

The global position vector of an arbitrary point of element i in the midsurface can be defined using the linear combination of the element-shape function matrix \mathbf{S} and the global nodal coordinate vector \mathbf{q} , which is given by

$$\mathbf{r} = \mathbf{S}(x, y)\mathbf{q}_i, \quad \mathbf{q}_i = \mathbf{B}_i\mathbf{q}, \quad (1)$$

Fig. 1 A thin rectangular plate element of ANCF (Color figure online)



where \mathbf{q}_i represents the element nodal coordinate vector, and x and y are the spatial coordinates defined in the element coordinate system, respectively. \mathbf{B}_i is a Boolean matrix. In the absolute nodal coordinate formulation, \mathbf{q}_i contains the global position vectors and slopes that are the spatial derivatives of the position vectors. The element nodal coordinate vector can be written as

$$\mathbf{q}_i = [\mathbf{q}_{i1}^T \quad \mathbf{q}_{i2}^T \quad \mathbf{q}_{i3}^T \quad \mathbf{q}_{i4}^T]^T, \tag{2}$$

where $\mathbf{q}_{ij} = [\mathbf{r}_{ij}^T \quad \mathbf{r}_{ij,x}^T \quad \mathbf{r}_{ij,y}^T \quad \mathbf{r}_{ij,xy}^T]^T$, $j = 1, \dots, 4$, and $\mathbf{r}_{ij,x} = \partial \mathbf{r}_{ij} / \partial x$, $\mathbf{r}_{ij,y} = \partial \mathbf{r}_{ij} / \partial y$, $\mathbf{r}_{ij,xy} = \partial^2 \mathbf{r}_{ij} / \partial x \partial y$.

In the classical theory of linear thermoelasticity, the thermal strain tensor is a linear relationship with temperature change [43, 44]. For a thin-plate structure, it is assumed that it causes only a positive strain but not a shear strain [45]. Considering a plate element whose temperature is raised from the reference temperature T_r at which strains and stresses are zero, to the temperature T , the thermal strain of the thin plate due to the temperature change $\Delta T = T - T_r$ is [43, 46] given by

$$\boldsymbol{\varepsilon}_T = \boldsymbol{\alpha}_T \Delta T = \begin{bmatrix} \alpha_x \\ \alpha_y \\ 0 \end{bmatrix} \Delta T, \tag{3}$$

where α_x and α_y are the coefficients of thermal expansion along the x and y directions, respectively.

Based on Kirchhoff assumptions, the virtual work done by the elastic force with thermoelasticity of the ANCF thin element i can be written as

$$\delta U_{ei} = \int_0^{a_e} \int_0^{b_e} \int_{-h/2}^{h/2} \delta \boldsymbol{\varepsilon}^T \mathbf{D} (\boldsymbol{\varepsilon} - \boldsymbol{\alpha}_T \Delta T) dz dy dx, \tag{4}$$

where \mathbf{D} represents the matrix of modulus, and $\boldsymbol{\varepsilon}$ represents the Green–Lagrange strain vector of an arbitrary point of the plate, which is given by

$$\boldsymbol{\varepsilon} = \boldsymbol{\varepsilon}_0 - z\boldsymbol{\kappa}, \tag{5}$$

where $\boldsymbol{\varepsilon}$ and $\boldsymbol{\kappa}$ represent the inplane Green-Lagrange strain vector and the curvature vector, respectively, which can be given as

$$\boldsymbol{\varepsilon}_0 = \begin{bmatrix} \frac{1}{2}(\mathbf{r}_x^T \mathbf{r}_x - 1) \\ \frac{1}{2}(\mathbf{r}_y^T \mathbf{r}_y - 1) \\ \mathbf{r}_x^T \mathbf{r}_y \end{bmatrix}, \quad \boldsymbol{\kappa} = \frac{1}{n} \begin{bmatrix} \mathbf{r}_{xx}^T \bar{\mathbf{n}} \\ \mathbf{r}_{yy}^T \bar{\mathbf{n}} \\ 2\mathbf{r}_{xy}^T \bar{\mathbf{n}} \end{bmatrix}, \tag{6}$$

where $\bar{\mathbf{n}}$ is a vector normal to the midsurface of the plate and n is the magnitude of $\bar{\mathbf{n}}$.

For an arbitrary point of the plate, the temperature change ΔT can be expressed with Taylor polynomials as

$$\Delta T(x, y, z, t) = T_0(x, y, t) + zT_1(x, y, t) + \dots + z^m T_m(x, y, t), \tag{7}$$

$$T_0(x, y, t) = \Delta T(x, y, 0, t),$$

$$T_k(x, y, t) = \left. \frac{\partial^k T(x, y, z, t)}{\partial z^k} \right|_{z=0} \quad (k = 1, \dots, m). \tag{8}$$

Considering that the thickness of the thin plate is small and the higher-order terms of Eq. (7) can be neglected, ΔT can be reduced as

$$\Delta T(x, y, z, t) = T_0(x, y, t) + zT_1(x, y, t). \tag{9}$$

Here, T_0 represents the temperature change of the midsurface of the thin plate and T_1 represents the temperature gradient along the thickness direction, which are obtained by solving the heat-conduction equations, as discussed later in Sect. 4.

Substituting Eqs. (5) and (9) into Eq. (4), the virtual work done by the elastic force can be rewritten as

$$\begin{aligned} \delta U_{ei} = & \int_0^{ae} \int_0^{be} \left(h\delta\boldsymbol{\varepsilon}_0^T \mathbf{D}\boldsymbol{\varepsilon}_0 + \frac{1}{12}h^3\delta\boldsymbol{\kappa}^T \mathbf{D}\boldsymbol{\kappa} \right) dydx \\ & - \int_0^{ae} \int_0^{be} h\delta\boldsymbol{\varepsilon}_0^T \mathbf{D}\boldsymbol{\alpha}_T T_0 dydx - \int_0^{ae} \int_0^{be} \frac{1}{12}h^3\delta\boldsymbol{\kappa}^T \mathbf{D}\boldsymbol{\alpha}_T T_1 dydx, \end{aligned} \tag{10}$$

Variation of $\boldsymbol{\varepsilon}_0$ and $\boldsymbol{\kappa}$ leads to

$$\delta\boldsymbol{\varepsilon}_0 = \mathbf{H}\delta\mathbf{q}_i, \quad \delta\boldsymbol{\kappa} = \mathbf{G}\delta\mathbf{q}_i, \tag{11}$$

$$\mathbf{H} = \begin{bmatrix} \mathbf{r}_x^T \mathbf{S}_x \\ \mathbf{r}_y^T \mathbf{S}_y \\ \mathbf{r}_x^T \mathbf{S}_y + \mathbf{r}_y^T \mathbf{S}_x \end{bmatrix}, \tag{12}$$

$$\mathbf{G} = \frac{1}{n} \begin{bmatrix} \mathbf{r}_{xx}^T \mathbf{Y} \\ \mathbf{r}_{yy}^T \mathbf{Y} \\ 2\mathbf{r}_{xy}^T \mathbf{Y} \end{bmatrix} + \frac{1}{n} \begin{bmatrix} \bar{\mathbf{n}}^T \mathbf{S}_{xx} \\ \bar{\mathbf{n}}^T \mathbf{S}_{yy} \\ 2\bar{\mathbf{n}}^T \mathbf{S}_{xy} \end{bmatrix} - \frac{1}{n^2} \boldsymbol{\kappa} \bar{\mathbf{n}}^T \mathbf{Y}, \tag{13}$$

$$\bar{\mathbf{n}} = \tilde{\mathbf{r}}_x \mathbf{r}_y, \quad \mathbf{Y} = \tilde{\mathbf{r}}_x \mathbf{S}_y - \tilde{\mathbf{r}}_y \mathbf{S}_x, \tag{14}$$

in which $\tilde{\mathbf{r}}_x$ and $\tilde{\mathbf{r}}_y$ are the 3×3 skew-symmetric matrices corresponding to \mathbf{r}_x and \mathbf{r}_y , respectively.

Substituting Eq. (11) into Eq. (10), the elastic force of the element is given by

$$\begin{aligned}
 \mathbf{Q}_{ei} &= (\partial U_{ei} / \partial \mathbf{q}_i)^T \\
 &= \int_0^{a_e} \int_0^{b_e} \left(h \mathbf{H}^T \mathbf{D} \boldsymbol{\varepsilon}_0 + \frac{1}{12} h^3 \mathbf{G}^T \mathbf{D} \boldsymbol{\kappa} \right) dy dx \\
 &\quad - \int_0^{a_e} \int_0^{b_e} \mathbf{H}^T \mathbf{D} \boldsymbol{\alpha}_T T_0 dy dx - \frac{1}{12} h^3 \int_0^{a_e} \int_0^{b_e} \mathbf{G}^T \mathbf{D} \boldsymbol{\alpha}_T T_1 dy dx.
 \end{aligned}
 \tag{15}$$

Accordingly, the elastic force can be written as

$$\mathbf{Q}_e = \sum_i \mathbf{B}_i^T \mathbf{Q}_{ei}.
 \tag{16}$$

Defining ρ as the mass density, \mathbf{g} as gravitational acceleration, and μ as the structural damping coefficient, the variational equations of motion read

$$\delta \mathbf{q}^T (\mathbf{M} \ddot{\mathbf{q}} + \mathbf{C} \dot{\mathbf{q}} + \mathbf{Q}_e - \mathbf{Q}_g) = 0,
 \tag{17}$$

where $\mathbf{M} = \sum \mathbf{B}_i^T (\int_0^{a_e} \int_0^{b_e} \rho h \mathbf{S}^T \mathbf{S} dy dx) \mathbf{B}_i$ is the constant generalized mass matrix, and $\mathbf{C} = \mu \mathbf{M}$ is the damping matrix, and $\mathbf{Q}_g = \sum \mathbf{B}_i^T (\int_0^{a_e} \int_0^{b_e} \rho h \mathbf{S}^T \mathbf{g} dy dx)$ is the generalized gravitational force vector.

3 Frictional contact formulations for a thin plate and a rigid body

In this study, two forms of contact are taken into account, i.e., plate-to-plate contact and plate-to-rigid body contact. This section derives two frictional contact elements on the basis of the ANCF thin-plate element, which can address multiple-point contact scenarios with large deformations and overall motions.

The normal contact is formulated using the penalty method [28, 30], and the tangential contact is modeled by the Coulomb friction law with a penalty regularization considering the stick–slip transition [29, 32]. The virtual work of the contact force is

$$\delta W_{cf} = \begin{cases} - \int_{\Omega} \delta \mathbf{u}_{cf}^T (\mathbf{f}_N + \mathbf{f}_T) d\Omega, & \text{if } g_N \leq 0, \\ 0, & \text{otherwise,} \end{cases}
 \tag{18}$$

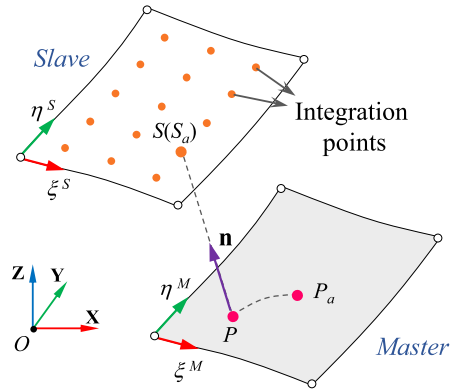
where g_N is the normal penetration, Ω is the contact area. \mathbf{u}_{cf} is the relative displacement vector of a contact pair, and $\mathbf{f}_N, \mathbf{f}_T$ are the normal and tangential force vectors of a contact pair, respectively. Contact between the contact pair occurs only if $g_N \leq 0$.

3.1 Contact between plates

Using the “master–slave” contact-detection approach [29], the contact is checked between each integration points of the slave and the master surfaces, which is named as the STS contact element. As shown in Fig. 2, the nodal vector for the STS contact element can be given by

$$\mathbf{q}_{ec} = [\mathbf{q}_{ec}^{mT} \quad \mathbf{q}_{ec}^{sT}]^T, \mathbf{q}_{ec}^m \in \mathbb{R}^{48 \times 1}, \mathbf{q}_{ec}^s \in \mathbb{R}^{48 \times 1}.
 \tag{19}$$

Fig. 2 Geometry and kinematics of the STS contact element (Color figure online)



The normal penetration can be defined as

$$g_N = (\mathbf{r}_S - \mathbf{r}_P)^T \mathbf{n} - \frac{h_M + h_S}{2}, \tag{20}$$

where h_M and h_S are the thicknesses of the master and slave surfaces, respectively. Following Eq. (14), the unit normal vector is obtained via the crossproduct of gradient vectors of the master surface, i.e., $\mathbf{n} = \bar{\mathbf{n}}/n$. Here, the direction of the unit normal vector is perpendicular to the master surface and points to the slave node [42, 47]. Thus, the variation of the relative displacement vector of the contact pair SP is written as

$$\delta \mathbf{u}_{cf} = \delta \mathbf{r}_S - \delta \mathbf{r}_P = \mathbf{S}_{cf} \delta \mathbf{q}_{ec}, \tag{21}$$

where \mathbf{S}_{cf} is the shape function matrix of the contact element, which can be defined as

$$\mathbf{S}_{cf} = [-\mathbf{S}_m(\xi^M, \eta^M) \quad \mathbf{S}_s(\xi^S, \eta^S)], \tag{22}$$

where \mathbf{S}_m and \mathbf{S}_s are the shape functions of the master and slave surfaces, respectively. ξ and η are the convective coordinates defined in the local surface-element coordinate system.

Based on the penalty method [28, 48], the normal contact force of the contact pair SP is formulated as

$$\mathbf{f}_N = \varepsilon_N g_N \mathbf{n}, \tag{23}$$

where ε_N is the normal penalty parameter.

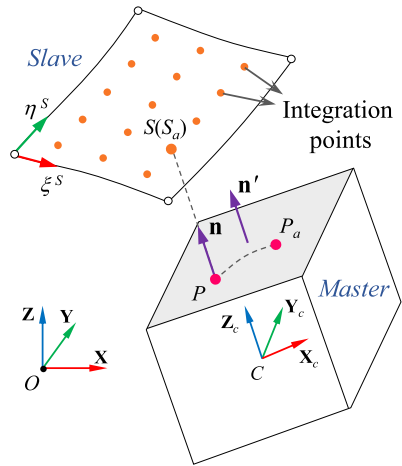
In order to describe the stick–slip transition, it requires the history variables from the previous step to describe the incremental nodal displacement [39]. Here, the points related to the previous step are represented by a subscript $(\cdot)_a$. As shown in Fig. 2, the contact point of the slave node S_a on the master surface is P_a in the previous step. Then, the incremental relative displacement vector of the contact pair SP is [42]

$$\Delta \mathbf{u}_{cf} = \Delta \mathbf{r}_S - \Delta \mathbf{r}_P, \tag{24}$$

where

$$\begin{aligned} \Delta \mathbf{r}_S &= \mathbf{0}, \\ \Delta \mathbf{r}_P &= \mathbf{S}_m(\xi_P^M, \eta_P^M) \mathbf{q}_{ec}^m - \mathbf{S}_{ma}(\xi_{P_a}^M, \eta_{P_a}^M) \mathbf{q}_{eca}^m. \end{aligned} \tag{25}$$

Fig. 3 Geometry and kinematics of STRS contact element (Color figure online)



Accordingly, the incremental relative displacement vector on the current tangential plane is

$$\mathbf{g}_T = (\mathbf{I}_3 - \mathbf{nn}^T) \Delta \mathbf{u}_{cf}. \tag{26}$$

The return-mapping scheme [32] for the Coulomb friction law with a penalty regularization is applied to measure the friction force, it introduces the trial tangential force vector as

$$\mathbf{f}_T^r = (\mathbf{I}_3 - \mathbf{nn}^T) \mathbf{f}_{Ta} - \varepsilon_T \mathbf{g}_T, \tag{27}$$

where \mathbf{f}_{Ta} is the real tangential force vector in the previous step, and ε_T is the tangential penalty parameter. According to the yield function of the Coulomb friction law [29], the real tangential force of the contact pair SP can be determined as

$$\mathbf{f}_T = \begin{cases} \mathbf{f}_T^r, & \text{if } \|\mathbf{f}_T^r\| - \mu_s \|\mathbf{f}_N\| \leq 0, \text{ sticking,} \\ \mu_d \|\mathbf{f}_N\| \frac{\mathbf{f}_T^r}{\|\mathbf{f}_T^r\|}, & \text{if } \|\mathbf{f}_T^r\| - \mu_s \|\mathbf{f}_N\| > 0, \text{ sliding,} \end{cases} \tag{28}$$

where μ_s and μ_d are the static and dynamic frictional coefficients, respectively.

Then, the element residual vector of the STS contact element can be summarized as

$$\mathbf{Q}_{ec}^{STS} = \int_{\Omega} \mathbf{S}_{cf}^T (\mathbf{f}_N + \mathbf{f}_T) d\Omega. \tag{29}$$

3.2 Contact between a plate and a rigid body

As shown in Fig. 3, the contact is checked between each integration points of the slave-plate surface and the master rigid surface, which is named as the STRS contact element. Thus, the nodal vector for the STRS contact element can be given by

$$\mathbf{q}_{ec} = [\mathbf{q}_c^T \quad \mathbf{q}_{ec}^{sT}]^T, \mathbf{q}_c \in \mathfrak{N}^{6 \times 1}, \mathbf{q}_{ec}^s \in \mathfrak{N}^{48 \times 1}. \tag{30}$$

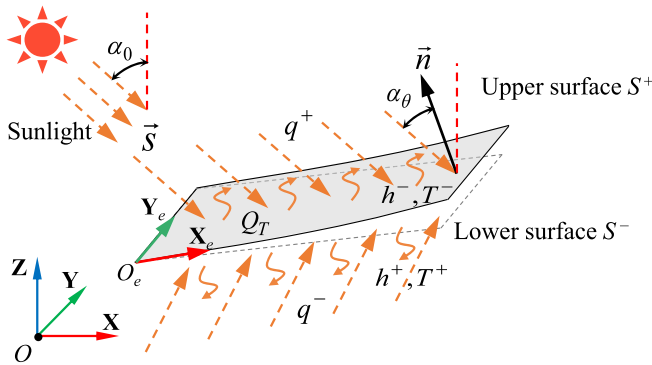


Fig. 4 A thin plate with large deformation and overall motion under solar radiation (Color figure online)

The normal penetration can be obtained by

$$g_N = (\mathbf{r}_S - \mathbf{r}_P)^T \mathbf{n} - \frac{h_M}{2}, \tag{31}$$

where $\mathbf{n} = \mathbf{A}_c \mathbf{n}'$ is the unit normal vector of the STRS contact element, and \mathbf{A}_c is the direction cosine of the rigid body, and \mathbf{n}' is the unit normal vector of the rigid surface, which is defined in the body-fixed frame $O_c\text{-}\mathbf{X}_c\mathbf{Y}_c\mathbf{Z}_c$. Then, the shape function matrix of the STRS contact element is

$$\mathbf{S}_{cf} = [-\mathbf{S}_m(\xi^M, \eta^M) \quad \mathbf{S}_s], \tag{32}$$

where $\mathbf{S}_s = [\mathbf{I}_3 \quad -\mathbf{A}_c \tilde{\rho}'_P \mathbf{K}_c]$ is the shape function of the slave rigid surface, ρ'_P is the position vector of the point P , which is defined in $O_c\text{-}\mathbf{X}_c\mathbf{Y}_c\mathbf{Z}_c$, and \mathbf{K}_c is a function of the Cardan orientation angle vector of $O_c\text{-}\mathbf{X}_c\mathbf{Y}_c\mathbf{Z}_c$ with respect to the inertial frame [51]. Similar to the STS contact element, the element residual vector of the STRS contact element can be obtained as

$$\mathbf{Q}_{ec}^{STRS} = \int_{\Omega} \mathbf{S}_{cf}^T (\mathbf{f}_N + \mathbf{f}_T) d\Omega. \tag{33}$$

Therefore, the generalized contact force vector related to Eq. (18) can be assembled as

$$\mathbf{Q}_{cf} = \sum_{n_{c1}} \mathbf{B}_e^{STS^T} \mathbf{Q}_{ec}^{STS} + \sum_{n_{c2}} \mathbf{B}_e^{STRS^T} \mathbf{Q}_{ec}^{STRS}, \tag{34}$$

where \mathbf{B}_e^{STS} and \mathbf{B}_e^{STRS} are the connectivity matrices of the STS and STRS contact elements, respectively. n_{c1} and n_{c2} are the numbers corresponding to STS and STRS contact elements, respectively.

4 Heat-conduction equations with solar radiation

As shown in Fig. 4, the thermal loads due to solar radiation are applied on a thin plate with large deformation and overall motion. According to the first law of thermodynamics and the

Fourier law of heat conduction [43–45], the variational heat-conduction equations for the three-dimensional continuum can be given by the authors’ previous study [13], as follows

$$\int_V (\rho c \delta T \dot{T} + \bar{k} \delta T_x T_x + \bar{k} \delta T_y T_y + \bar{k} \delta T_z T_z - Q_T) dV - \int_{S^+} \delta T q^+ dS - \int_{S^-} \delta T q^- dS = 0, \tag{35}$$

where c is the specific heat of the material, \bar{k} is the thermal conductivity, Q_T is the intensity of the heat source, and q^+ , q^- represent the heat flux of the upper and lower surfaces, respectively.

Since the distribution of solar-radiation input is affected by various factors, including its position, attitude, and configuration, the absorption of incident solar rays needs to be further evaluated by the heat flux [27]. The solar unit vector is defined as \vec{s} , the angle of incidence is α_θ , and the initial angle of incidence is α_0 . Taking into account the effect of the shadow region, q^+ and q^- can be given by

$$\begin{aligned} q^+ &= c_s \alpha_m^+ \xi^+ S_0 - \sigma \zeta^+ (T^+)^4, \\ q^- &= c_s \alpha_m^- \xi^- S_0 - \sigma \zeta^- (T^-)^4. \end{aligned} \tag{36}$$

where S_0 is the solar-radiation heat flux, c_s is the solar coefficient related to the shadow region, α_m^+ , α_m^- represent the effective solar absorptivity of the upper and lower surfaces, respectively, ξ^+ , ξ^- represent the albedo view factors of the upper and lower surfaces, respectively, σ represents the Stefan–Boltzmann constant, ζ^+ , ζ^- represent the emissivity of the upper and lower surfaces, respectively, and $T^+ = T_r + \Delta T^+$, $T^- = T_r + \Delta T^-$ represent the absolute temperature of the upper and lower surfaces, respectively. When the plate is in a shadow region, $c_s = 0$.

Considering the influence of rigid-body motion and elastic deformation on the albedo view factors of the upper and lower surfaces, the albedo view factors are given by [2, 13]

$$\xi^\pm = \begin{cases} \cos \alpha_\theta^\pm, & 0 \leq \alpha_\theta^\pm \leq \pi/2, \\ 0, & \pi/2 < \alpha_\theta^\pm \leq \pi, \end{cases} \quad \xi^\pm = \begin{cases} \cos \alpha_\theta^\pm, & 0 \leq \alpha_\theta^\pm \leq \pi/2, \\ 0, & \pi/2 < \alpha_\theta^\pm \leq \pi, \end{cases} \tag{37}$$

where α_θ^+ and α_θ^- are given by

$$\alpha_\theta^\pm = \arccos \left(-\frac{1}{n^\pm} (\bar{\mathbf{n}}^\pm)^T \mathbf{s} \right), \quad \alpha_\theta^\pm = \arccos \left(-\frac{1}{n^\pm} (\bar{\mathbf{n}}^\pm)^T \mathbf{s} \right), \tag{38}$$

where the normal vectors are

$$\bar{\mathbf{n}}^+ = \bar{\mathbf{r}}_x^+ \mathbf{r}_y^+, \quad \bar{\mathbf{n}}^- = \bar{\mathbf{r}}_x^- \mathbf{r}_y^-. \tag{39}$$

Since $\bar{\mathbf{n}}^+$ and $\bar{\mathbf{n}}^-$ are closely related to the attitude motion of the rigid body as well as the elastic deformation of the plate, the present formulation considers the influence of the attitude motion and the structural deformation on the heat flux q^+ and q^- , which is a complete rigid–flexible–thermal coupling model.

However, in the conventional formulation, with the neglect of the effects of rigid-body motion and elastic deformation on the heat flux, α_θ^+ and α_θ^- are assumed to be constant,

which can be expressed as $\alpha_{\theta}^{+}(t) = \alpha_{\theta}^{+}(0) = \alpha_0$, $\alpha_{\theta}^{-}(t) = \alpha_{\theta}^{-}(0) = \pi - \alpha_0$. In this case, it is not a complete rigid–flexible–thermal coupling model.

By means of Taylor polynomials, the three-dimensional temperature field of a thin plate can be described by the change of the midsurface temperature T_0 and the temperature gradient along the thickness direction T_1 . Using a finite-element method, T_0 and T_1 can be discretized as [49]

$$T_k = \mathbf{N}\mathbf{p}_{ik} \quad (k = 0, 1), \tag{40}$$

where \mathbf{p}_{ik} ($k = 0, 1$) represent the vectors of temperature variables of plate element i , and \mathbf{N} represents the shape-function matrix. Defining \mathbf{p}_k ($k = 0, 1$) as the global vectors of temperature variables, the relation between the element vector and the global vector can be given by $\mathbf{p}_{ik} = \mathbf{B}_{ik}\mathbf{p}_k$ ($k = 0, 1$). Substituting Eq. (40) into Eq. (9), the absolute temperature in Eq. (35) can be expressed as

$$T = T_r + \Delta T = T_r + T_0 + zT_1 = T_r + \mathbf{N}\mathbf{B}_{i0}\mathbf{p}_0 + \mathbf{N}\mathbf{B}_{i1}\mathbf{p}_1. \tag{41}$$

Accordingly, the variational heat-conduction equations can be rewritten as

$$\delta \mathbf{p}^T (\mathbf{M}_T \dot{\mathbf{p}} + \mathbf{K}_T \mathbf{p} - \mathbf{F}_T) = 0, \tag{42}$$

where

$$\mathbf{p} = \begin{bmatrix} \mathbf{p}_0 \\ \mathbf{p}_1 \end{bmatrix}, \mathbf{M}_T = \begin{bmatrix} \mathbf{M}_0 & \mathbf{0} \\ \mathbf{0} & \mathbf{M}_1 \end{bmatrix}, \mathbf{K}_T = \begin{bmatrix} \mathbf{K}_0 & \mathbf{0} \\ \mathbf{0} & \mathbf{K}_1 \end{bmatrix}, \mathbf{F}_T = \begin{bmatrix} \mathbf{F}_0 \\ \mathbf{F}_1 \end{bmatrix}, \tag{43}$$

$$\mathbf{M}_k = b_k \int_0^{a_e} \int_0^{b_e} \rho c \mathbf{N}^T \mathbf{N} dy dx, \quad (k = 0, 1), \tag{44}$$

$$\mathbf{K}_k = b_k \int_0^{a_e} \int_0^{b_e} \bar{k} (\mathbf{N}_x^T \mathbf{N}_x + \mathbf{N}_y^T \mathbf{N}_y) dy dx + kh \int_0^{a_e} \int_0^{b_e} \bar{k} \mathbf{N}^T \mathbf{N} dy dx, \quad (k = 0, 1), \tag{45}$$

$$\begin{aligned} \mathbf{F}_k &= b_k \int_0^{a_e} \int_0^{b_e} Q_T \mathbf{N}^T dy dx + \int_0^{a_e} \int_0^{b_e} (0.5h)^k q^+ \mathbf{N}^T dy dx \\ &+ \int_0^{a_e} \int_0^{b_e} (-0.5h)^k q^- \mathbf{N}^T dy dx, \quad (k = 0, 1), \end{aligned} \tag{46}$$

$$b_k = \int_{-h/2}^{h/2} z^k dz, \quad (k = 0, 1). \tag{47}$$

Considering that the temperature variable vector \mathbf{p} is independent, the heat-conduction equations are given by

$$\mathbf{M}_T \dot{\mathbf{p}} + \mathbf{K}_T \mathbf{p} - \mathbf{F}_T = \mathbf{0}. \tag{48}$$

5 Dynamic equations for the rigid–flexible–thermal coupling multibody system

Defining $\mathbf{q}_c = [\mathbf{r}_c^T \quad \boldsymbol{\theta}_c^T]^T$ as the generalized coordinate vector of the rigid body, where \mathbf{r}_c is the position vector of the centroid defined in the inertial frame, and $\boldsymbol{\theta}_c$ is the Cardan

orientation angle vector of $O_c\text{-}X_cY_cZ_c$ with respect to the inertial frame. In addition, the mass matrix \mathbf{M}_c and the generalized force vector \mathbf{Q}_c of the rigid body are detailed in [50, 51].

Combining the constraint equations $\Phi(\mathbf{q}_c, \mathbf{q}, t) = \mathbf{0}$, the rigid–flexible coupling dynamics equations [52] and the heat-conduction equations, the mixed differential-algebraic equations for the rigid–flexible–thermal coupling multibody system are given by

$$\Psi = \begin{bmatrix} \mathbf{M}_d \ddot{\mathbf{q}}_d + \mathbf{C}_d \dot{\mathbf{q}}_d + \Phi_{\mathbf{q}_d}^T \lambda - \mathbf{Q}_d(\mathbf{p}) \\ \Phi \\ \mathbf{M}_T \dot{\mathbf{p}} + \mathbf{K}_T \mathbf{p} - \mathbf{F}_T(\mathbf{q}_d) \end{bmatrix} = \mathbf{0}, \tag{49}$$

where the generalized coordinate vector of the system is $\mathbf{q}_d = [\mathbf{q}_c^T \quad \mathbf{q}^T]^T$, and the generalized mass matrix \mathbf{M}_d , damping matrix \mathbf{C}_d , and force matrix \mathbf{Q}_d take the form

$$\mathbf{M}_d = \begin{bmatrix} \mathbf{M}_c & \mathbf{0}_{6 \times n_q} \\ \mathbf{0}_{n_q \times 6} & \mathbf{M} \end{bmatrix}, \tag{50}$$

$$\mathbf{C}_d = \begin{bmatrix} \mathbf{0}_{6 \times 6} & \mathbf{0}_{6 \times n_q} \\ \mathbf{0}_{n_q \times 6} & \mathbf{C} \end{bmatrix}, \tag{51}$$

$$\mathbf{Q}_d = \begin{bmatrix} \mathbf{Q}_c \\ \mathbf{Q}_g - \mathbf{Q}_e \end{bmatrix} + \mathbf{Q}_{cf}, \tag{52}$$

where n_q is the number of the generalized coordinates of the plate, and λ is the vector of the Lagrange multiplier corresponding to the constraint equations.

A new numerical approach combining the generalized- α method and the modified central-difference method is proposed to solve the strong rigid–flexible–thermal coupling equations. The dynamic equations are solved by the generalized- α method [53, 54], and the heat-conduction equations are solved by a modified central-difference method [49]. Then, the Newton–Raphson algorithm is adopted to solve the combined nonlinear algebraic equations. The solution procedure can be divided into three steps, which are presented in detail in the Appendix.

Figure 5 shows the computational flowchart of the new numerical method proposed in this paper. Compared with the fourth-order Runge–Kutta method used uniformly in the authors’ previous study [13], the computational efficiency of this proposed method is significantly improved. Additionally, compared with the traditional uncoupled method, this method ensures the accuracy of the full coupled simulation by solving the heat-conduction equations and the dynamic equations simultaneously. Considering the geometric nonlinearities (large deformation) and boundary nonlinearities (frictional contact), the variable-step-size control scheme [55] and the preconditioning strategy are employed to improve efficiency.

6 Validations

In this section, in order to verify the correctness of the proposed thermal–structural coupling model, simulation experiments of a plate clamped at two sides and a cantilevered plate applied with thermal loads are carried out, while the results from the commercial finite-element software ABAQUS are taken as benchmarks.

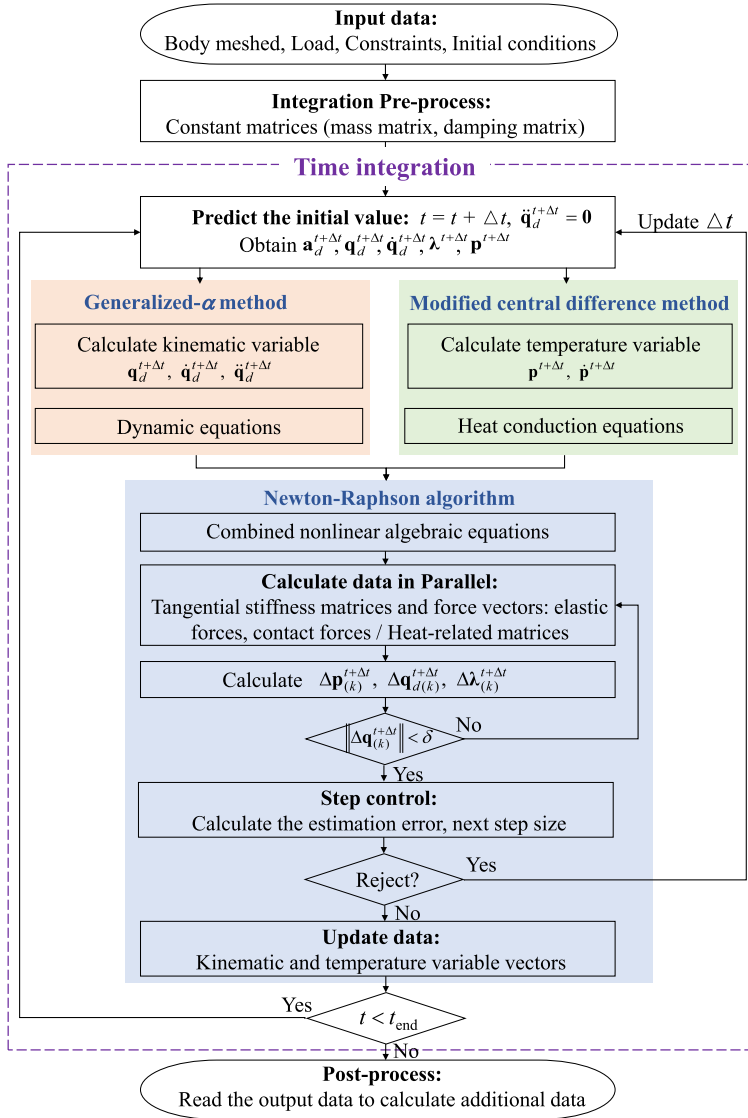


Fig. 5 Computational flowchart for the proposed numerical approach (Color figure online)

6.1 Simulation of a plate clamped at two sides

As shown in Fig. 6, two sides of a plate are fixed on the inertial reference frame $O - \mathbf{XYZ}$, and a constant heat flux q_T is applied to the upper surface of the plate. The initial temperature of the whole plate is set at 0 K. The geometric properties and material data of the plate are: length $l = 4$ m, width $b = 2$ m, thickness $h = 0.01$ m, mass density $\rho = 36.8$ kg/m³, elastic modulus $E = 1.93 \times 10^9$ Pa, Poisson ratio $\nu = 0.3$, thermal-expansion coefficient $\alpha_x = \alpha_y = 2.3 \times 10^{-5}$ (1/K), conductivity coefficient $\bar{k} = 1.5$ W/(m · K), and specific heat

Fig. 6 A plate clamped at two sides in a thermal environment (Color figure online)

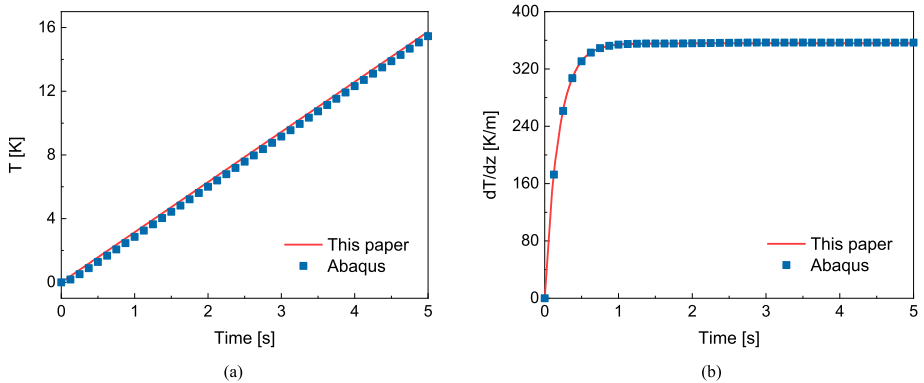
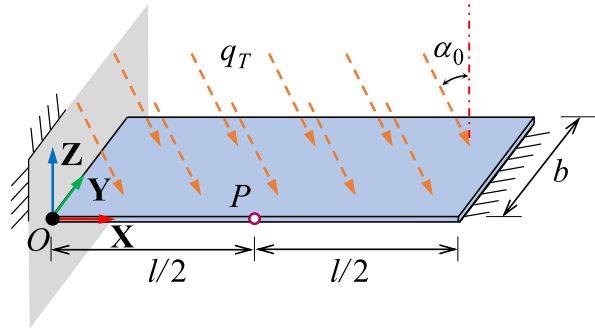


Fig. 7 Time histories of (a) midsurface temperature of point P ; (b) temperature gradient of point P in the z direction (Color figure online)

$c = 921 \text{ J}/(\text{kg} \cdot \text{K})$. In this simulation, the heat flux of the upper and lower surfaces are $q^+ = q_T \cos \alpha_0$ and $q^- = 0$, respectively, where $q_T = 1067 \text{ W}/\text{m}^2$ and $\alpha_0 = 0$.

As shown in Fig. 7, the time histories of the midsurface temperature of point P and the temperature gradient $T_1 = \partial T / \partial z$ of point P are given, and the results are in good agreement with the comparative results provided by ABAQUS, which demonstrates that the temperature field can be calculated precisely by the proposed method.

To further investigate the geometric nonlinear effects, the deflections of point P in the z direction using linear and nonlinear models are compared in Fig. 8. Since the two edges of the plate are fixed, the thermal load leads to compressive thermal stress. It is found that for the nonlinear model, the thermal force causes the softening of the plate, which induces large transverse deformations. However, the results obtained by the linear model are quite different. Due to the neglect of the nonlinear stiffness matrices, the softening effect is not shown and the transverse deformation is small. Furthermore, the results of this paper coincide with the results achieved by ABAQUS, which validates the effectiveness of the proposed thermal integrated ANCF thin-plate element in terms of geometric nonlinearity.

6.2 Simulation of a cantilevered plate

As shown in Fig. 9, the dynamic simulation of a cantilevered plate applied with thermal loads is performed. The geometric properties and material data of the plate are the same

Fig. 8 Time history of the deflection of point P in the z direction (Color figure online)

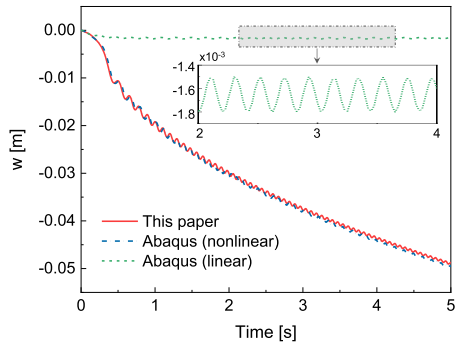


Fig. 9 A cantilevered plate in a thermal environment (Color figure online)

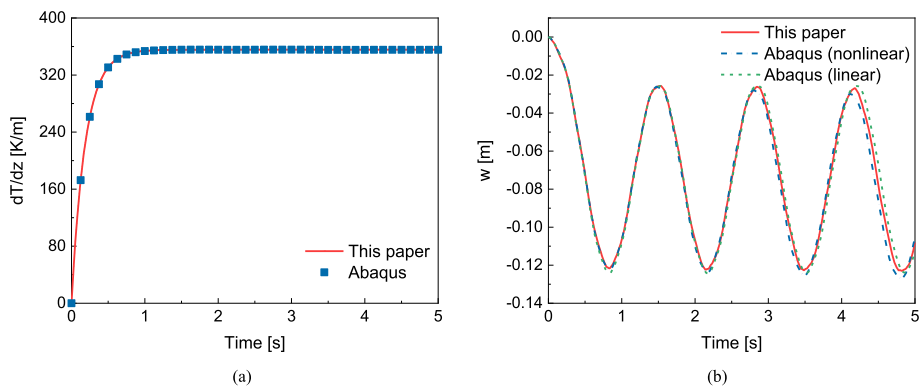
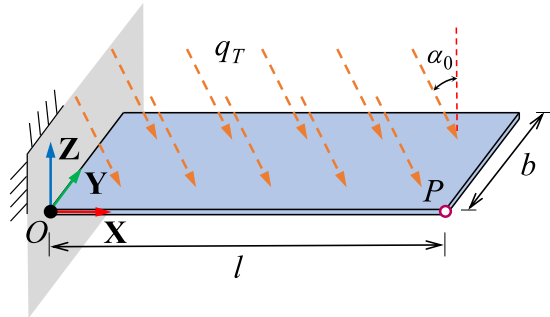


Fig. 10 Time histories of (a) temperature gradient; (b) deflection of point P in the z direction (Color figure online)

as the numerical example 6.1. The time history of the temperature gradient of point P in the z direction is given in Fig. 10(a), which shows that the results are in accordance with the results obtained by ABAQUS. From the results of the deflections of point P in the z direction shown in Fig. 10(b), we can obtain that the results of the linear and nonlinear models coincide well, it can be concluded that for cantilevered plate without tip constraint, the use of a linear model is computationally accurate and efficient.

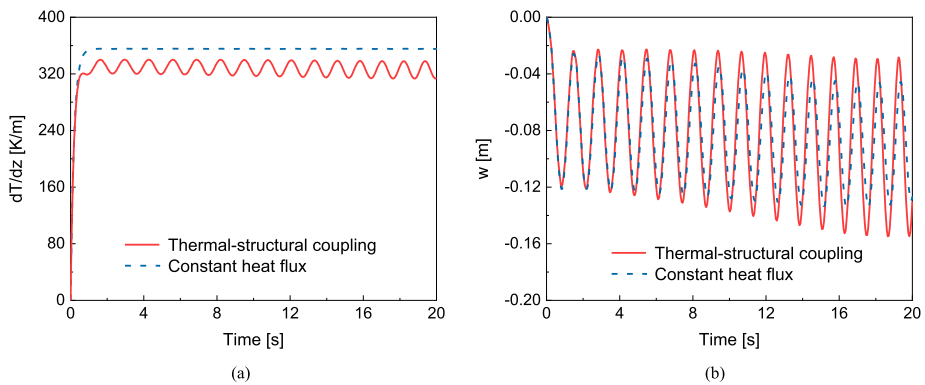


Fig. 11 Time histories of (a) temperature gradient; (b) deflection of point P in the z direction (Color figure online)

The thermal–structural analysis for the cantilevered plate applied with thermal loads is further conducted through a comparative study of the thermal–structural coupling model and the constant heat flux model, where $q_T = 2525 \text{ W/m}^2$ and $\alpha_0 = 65^\circ$, which ensures that $q^+ = 1067 \text{ W/m}^2$. The time histories of the temperature gradient and the deflection of point P in the z direction are shown in Fig. 11, respectively. As can be seen in the figures, due to the neglect of the elastic deformation of the constant heat-flux model, such a model cannot reveal the thermally induced vibration effect, therefore the vibration amplitude of the temperature gradient and the deflection is constant. On the contrary, since the heat flux varies with the deformation of the plate, the vibration amplitudes of the temperature gradient and the deflection obtained by the thermal–structural coupling model keep increasing. In summary, the proposed model takes into account the coupling effect of the heat flux and the elastic deformation, so that it is able to capture the phenomenon of thermally induced vibration, which is hardly achieved in the commercial finite element software ABAQUS.

7 Numerical simulations of a satellite and solar-array multibody system in a thermal environment

Thermal–dynamic analysis of the solar array is of vital importance to the safe operation of spacecraft. In this section, we present two numerical examples to demonstrate the effectiveness of the proposed rigid–flexible–thermal coupling model for the satellite and solar-array multibody system in a thermal environment. The first numerical example focuses on comparing the different coupling models to reveal the dynamic characteristics of thermally induced vibration. The other numerical example is employed to analyze the deployment dynamic performance of the solar array considering contact and thermal loading.

7.1 Numerical simulation of a satellite and solar-array system in a thermal environment

A satellite and solar-array system applied with solar radiation is shown in Fig. 12. The flexible solar array is fully deployed, and its left edge is fixed to the rigid satellite. In this simulation example, the rigid satellite is a cube, and the solar array is an isotropic flexible

Fig. 12 A satellite and solar-array system (Color figure online)

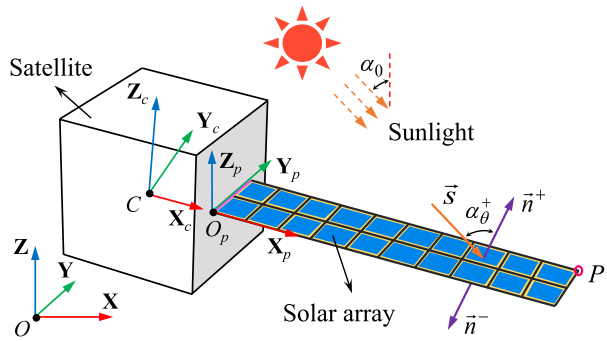


Table 1 Geometric and material properties

<i>Satellite</i>	Size of the rectangular satellite	2 m × 2 m × 2 m
	Mass	2000 kg
	Inertia matrix in body-fixed frame	$J_x = J_y = J_z = 200 \text{ kg} \cdot \text{m}^2$
	Length	$L^P = 8 \text{ m}$
	Width	$W^P = 1 \text{ m}$
	Thickness	$h = 0.01 \text{ m}$
	Elastic modulus	$E = 1.93 \times 10^9 \text{ Pa}$
	Poisson's ratio	$\gamma = 0.3$
	Mass density	$\rho = 36.8 \text{ kg/m}^3$
	Damping coefficient	$\mu = 0.0001 \text{ (1/s)}$
	Thermal expansion coefficient	$\alpha_x = \alpha_y = 2.3 \times 10^{-5} \text{ (1/K)}$
	Specific heat of the plate	$c = 921 \text{ J/(kg} \cdot \text{K)}$
	<i>Solar array</i>	Initial angle of incidence
Thermal conductivity		$\bar{k} = 1.5 \text{ W/(m} \cdot \text{K)}$
Solar heat flux		$S_0 = 1350 \text{ W/m}^2$
Solar absorptivity of the plate		$\alpha_m = 0.79$
Intensity of heat source		$Q_T = 0$
Stefan–Boltzmann constant		$\sigma = 5.67 \times 10^{-8} \text{ W/(m}^2 \cdot \text{K}^4)$
Emissivity of the upper surface		$\zeta^+ = 0.7$
Emissivity of the lower surface		$\zeta^- = 0.7$
Gravitational acceleration		$g = 0$

plate. The inertial reference frame $O\text{--}XYZ$ is established at the centroid C of the rigid satellite, and the geometric and material properties are given in Table 1.

Defining the initial angle of incidence α_0 as the solar angle, the coordinate vector of the solar sunlight is given by $\mathbf{s} = [\sin \alpha_0 \quad 0 \quad -\cos \alpha_0]^T$. Initially, the satellite is in a static state, and the body-fixed frame of the satellite is parallel to the global coordinate system. The reference temperature is 273 K.

7.1.1 Dynamic performance of an orbit satellite and solar-array system

To reveal the advantages of the rigid–flexible–thermal coupling model proposed in this paper for the satellite and solar-array system, two dynamic models are compared: the complete

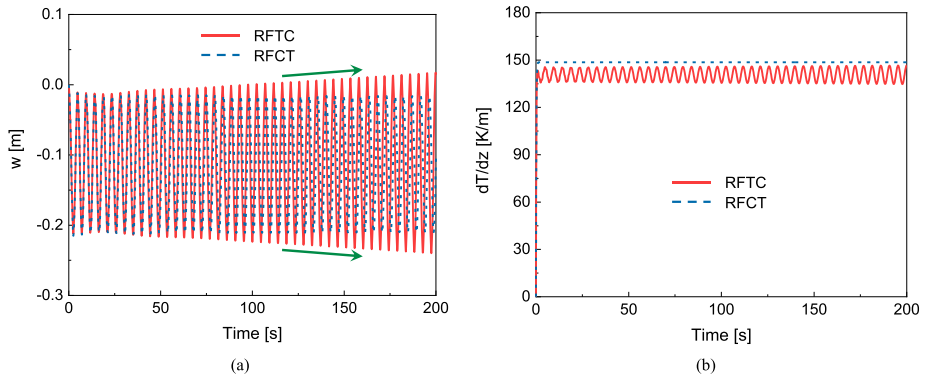


Fig. 13 Time histories of (a) deflection of point P in the z_c direction; (b) temperature gradient of point P in the z direction (Color figure online)

rigid–flexible–thermal coupling model (RFTC) and the rigid–flexible coupling model considering the thermal effect (RFCT). In the RFTC formulation, α_θ^+ and α_θ^- are closely related to $\mathbf{q}_d^{t+\Delta t}$. However, in the RFCT formulation, α_θ^+ and α_θ^- are assumed to be constant, which are equal to α_0 and $\pi - \alpha_0$, respectively, and thus the temperature results are not influenced by the rigid-body motion and the elastic deformation.

For a more intuitive description of the deformation, deflection is introduced. The deflection of an arbitrary point on the plate can be written as

$$\mathbf{u} = [u \quad v \quad w]^T = \mathbf{A}_p^T (\mathbf{r} - \mathbf{r}_0), \tag{53}$$

where \mathbf{r}_0 is the origin of the body-fixed frame of the plate, and \mathbf{A}_p is the transformation matrix of the body-fixed frame with respect to the inertial frame.

The time histories of the deflection of the corner point P in the z_c direction and the temperature gradient $T_1 = \partial T / \partial z$ of the corner point P are shown in Figs. 13(a) and (b), respectively. As can be seen in the figures, due to ignoring the coupling effect of the solar heat flux, the rigid-body motion, and the elastic deformation, the RFCT model cannot reveal the thermally induced vibration. Accordingly, the vibration amplitude of the deflection is constant. On the contrary, the vibration amplitudes of the deflection and the temperature gradient obtained by the RFTC model keep increasing, which explains the phenomenon of the thermally induced vibration effect.

In order to further analyze the effect of thermal load on the motion of the satellite, Fig. 14 gives the time histories of the centroidal velocity of the satellite in the z direction and the angular velocity of the satellite in the y_c direction. Due to the coupling of the translational and the rotational motion of the satellite and the elastic deformation of the solar array, the vibration amplitudes of the angular velocity and the centroidal velocity of the satellite obtained by the RFTC model also keep increasing. In summary, it reveals that the thermally induced vibration phenomenon is obvious in practical engineering and needs to be paid attention to.

7.1.2 Parameter analysis of thermally induced vibration

In this section, based on the proposed rigid–flexible–thermal coupling model, some characteristic parameters are investigated: the solar angle α_0 , the specific heat c of the plate, and the damping coefficient μ of plate on the thermally induced vibration effect.

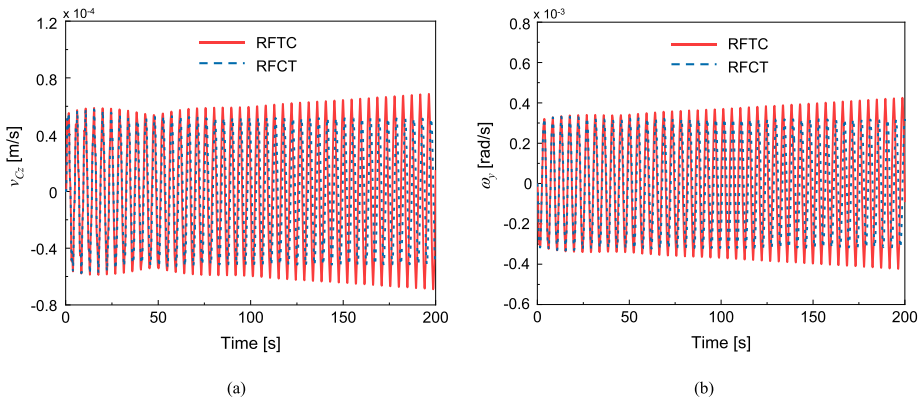


Fig. 14 Time histories of (a) centroidal velocity of the satellite in the z direction; (b) angular velocity of the satellite in the y_c direction (Color figure online)

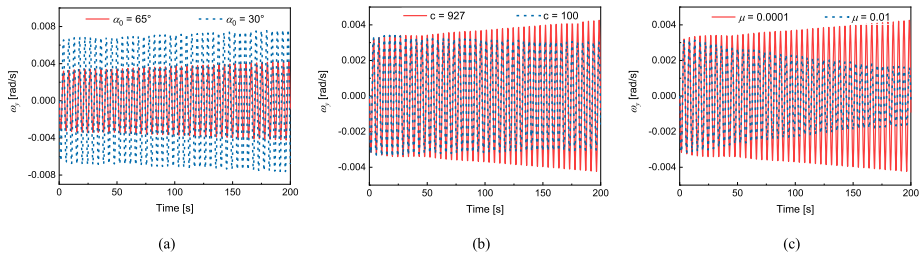


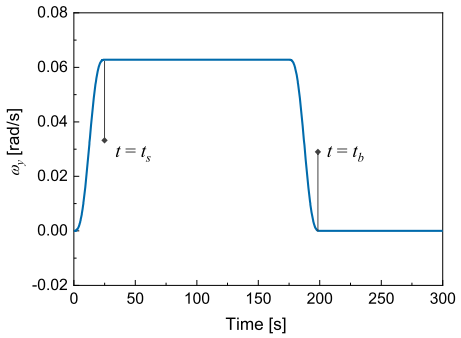
Fig. 15 Time histories of the angular velocity of the satellite in the y_c direction: under different (a) solar angles α_0 ; (b) plate specific heats c ; (c) plate damping coefficients μ (Color figure online)

According to the change of the solar angle, the time history of the angular velocity of the satellite in the y_c direction is shown in Fig. 15(a). It is indicated that with the decrease of the solar angle, the average of the deflection increases because of the increase of the intensity of the solar heat flux. However, the variation of the solar heat flux caused by the angular deformation of the plate and the rotation of the satellite becomes less significant, therefore, the thermally induced vibration due to the rigid–flexible–thermal coupling effect also decreases.

Figure 15(b) depicts the time history of the angular velocity of the satellite in the y_c direction at different plate specific heats. As can be seen in the figure, due to the decrease of c and the increase of the thermal coefficient $\bar{k}/(\rho c)$, the thermally induced vibration also weakens.

The time history of the angular velocity of the satellite in the y_c direction under different plate damping coefficients is compared, as shown in Fig. 15(c). It can be seen that with the increase of the structural damping coefficient, the vibration amplitude of the deflection attenuates applied with the damping force, which indicates that the increase of the structural damping coefficient contributes to weakening the thermally induced vibration.

Fig. 16 Time history of ω_y (Color figure online)



7.1.3 Dynamic performance of a maneuvering satellite and solar-array system

In this section, the nonlinear dynamic performance of the maneuvering satellite and solar-array system applied with a thermal load is investigated. Additionally, the solar heat flux is applied on the plate, and the satellite is applied with a translational constraint, which is given by $x_c = 0, y_c = 0, z_c = 0$, and a rotational constraint, which is given by $\omega_x = 0, \omega_z = 0$, and

$$\omega_y = \begin{cases} \frac{\omega_s}{t_s} \left(t - \frac{t_s}{2\pi} \sin \frac{2\pi t}{t_s} \right), & 0 \leq t < t_s, \\ \omega_s, & t_s \leq t < t_b - t_s, \\ \frac{\omega_s}{t_s} \left(t_b - t - \frac{t_s}{2\pi} \sin \frac{2\pi (t_b - t)}{t_s} \right), & t_b - t_s \leq t < t_b, \\ 0, & t > t_b, \end{cases} \quad (54)$$

where $t_b = 200$ s, $t_s = t_b/8$, $\omega_s = \pi/50$, which is shown in Fig. 16.

On the basis of the RFTC model proposed in this paper, the deformed configurations of the satellite and solar-array multibody system as well as the distribution of the von Mises stress of the solar array at some time steps are depicted in Fig. 17. Initially, the satellite rotates with angular velocity around the y_c -axis, which in turn drives the motion of the solar array. In this situation, the solar array undergoes large deformations and overall motions. It is shown that the stress concentration mainly occurs at the roots of the solar array, and the stress wave gradually spreads toward the free edge of the solar array.

For the purpose of highlighting the advantages of the rigid–flexible–thermal coupling model for dynamic analysis of the maneuvering satellite and solar-array system with large deformations and overall motions, three dynamic models are compared: the RFTC model, the RFCT model, and the rigid–flexible coupling model without considering the thermal effect (RFC). In the RFC formulation, only rigid–flexible coupling effects are considered, while thermal effects are ignored.

Figure 18 gives the time histories of the deflection w of the corner point P in the z_c direction and the temperature gradient $T_1 = \partial T / \partial z$ of the corner point P , respectively. As can be seen in the figure, in the RFC model, except for the acceleration and deceleration phases of ω_y , the deflection of point P in the z_c direction maintains a small-amplitude vibration due to the rigid–flexible coupling effect. For $t < 200$ s, the satellite undergoes periodic rotational motion in the y direction, which leads to the periodic deflection in the z_c direction and the periodic variation of the temperature gradient in the thickness direction due to the complete rigid–flexible–thermal coupling effect, while the deflection and the temperature gradient

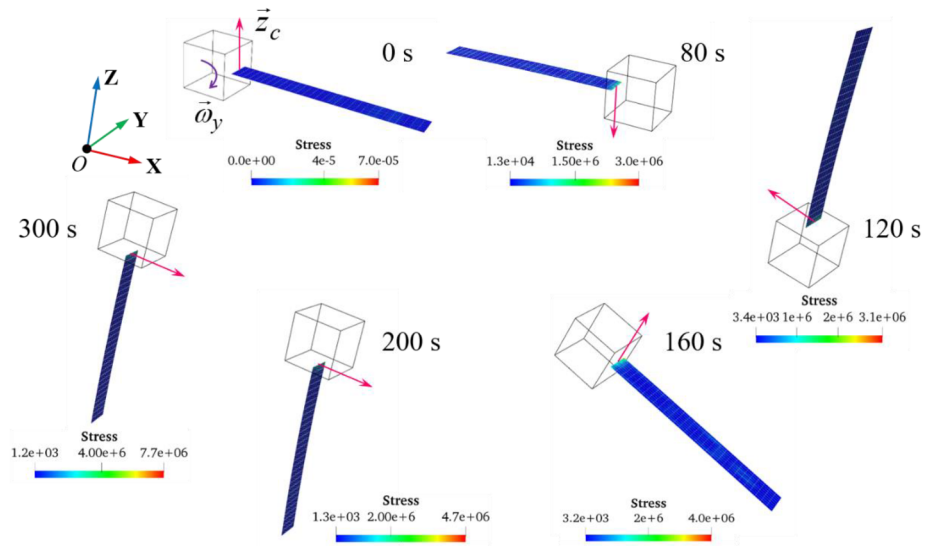


Fig. 17 Motion of the satellite and solar-array system at some time steps (Color figure online)

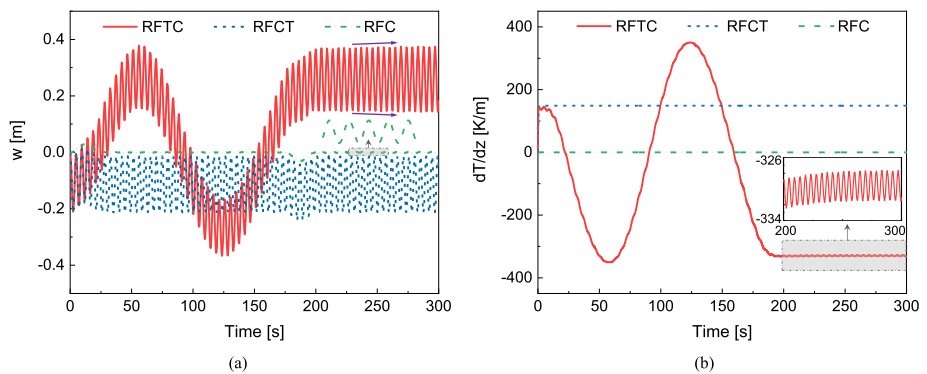


Fig. 18 Time histories of (a) deflection of point P in the z_c direction; (b) temperature gradient of point P in the z direction (Color figure online)

obtained by the RFCT model shows neither periodic variation nor amplitude growing. Furthermore, it is shown that for $t > 200$ s, with the release of the applied angular velocity ω_y , the amplitude of vibration obtained by the RFTC model keeps increasing slowly, which reveals the phenomenon of the thermally induced vibration.

To further analyze the thermal-dynamic performance of the maneuvering satellite and solar-array system, Fig. 19 gives the phase diagrams of point P in different models. From the phase diagram in the RFC model, it can be seen that the trajectory of the phase diagram exhibits a periodic motion without vibration under the action of ω_y . In the RFCT model, the trajectory of the phase diagram can be viewed as the thermal vibrations superimposed on the basis of the RFC model. Since the thermal loads are assumed to be constant in the RFCT model, the thermal vibrations appear as low-frequency oscillations. However, in the RFTC model, it shows low-frequency periodic motion as well as the high-frequency thermally

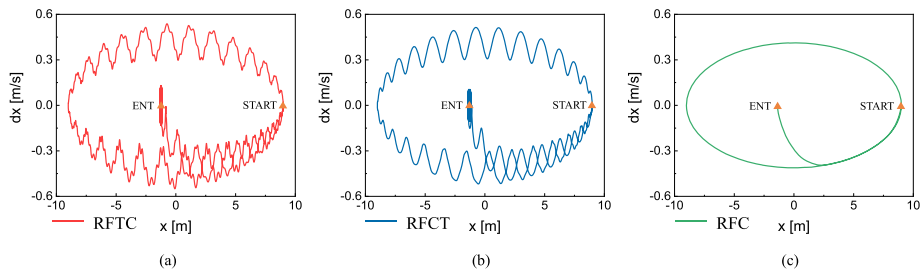


Fig. 19 Phase diagrams point P in (a) RFTC model; (b) RFCT model; (c) RFC model (Color figure online)

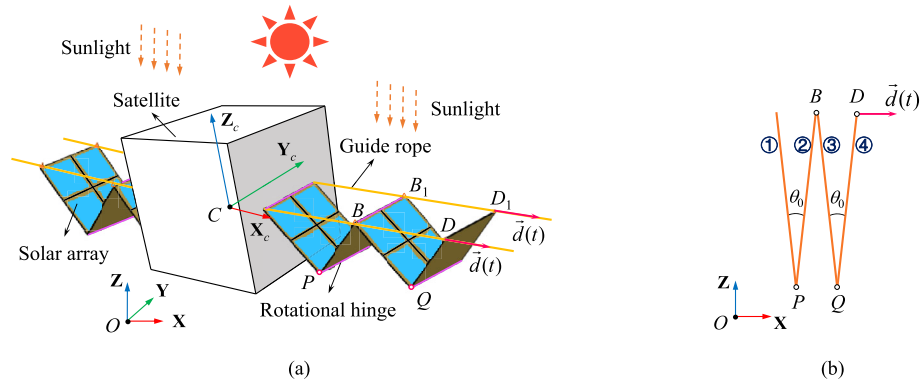


Fig. 20 A simplified model of the deployment satellite and solar-array system in a thermal environment: (a) partially deployed configuration; (b) stowed configuration (Color figure online)

induced vibration, due to the consideration of the influences of rigid-body motion and elastic deformation on the intensity of solar radiation. Therefore, it is necessary to adopt the more precise rigid–flexible–thermal coupling model for dynamic analysis of maneuvering satellite and solar-array systems, which can capture richer nonlinear characteristics.

7.2 Deployment dynamics of a solar array in a thermal environment with frictional contact

The second example deals with the deployment of the solar array in a thermal environment considering frictional contact. The simplified model of the satellite and solar-array system in a thermal environment is illustrated by Fig. 20, which consists of four guide wires, eight solar panels, and eight rotational hinges. It is worth mentioning that the translational and attitude motion of the satellite is controlled during the deployment of the solar array, and it can be regarded as points B , D , B_1 , and D_1 are restricted to move on the guide wires ignoring the deformation of the guide wires. Since the direction of sunlight is along the negative z -axis, and the solar array are symmetrically distributed about the central satellite, it is sufficient to analyze the deployment of the solar panels on one side. $O-XYZ$ is the inertial reference frame, which is consistent with the body-fixed frame of the satellite $C-X_cY_cZ_c$.

The length of one side of the solar array is $L^P = 5$ m, and the solar angle $\alpha_0 = 0$, and for the other geometric and material properties refer to Table 1. The initial angle between

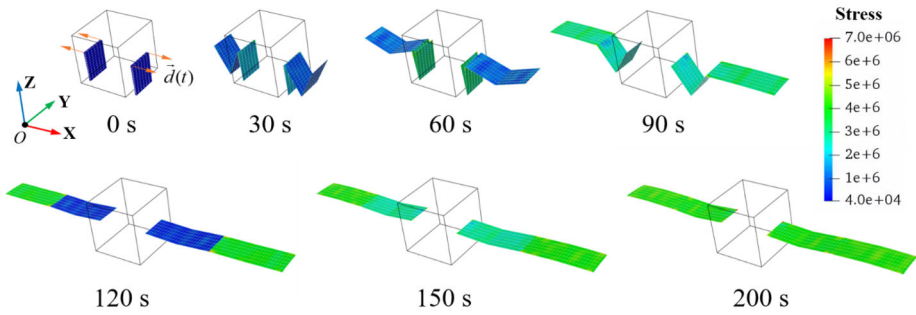


Fig. 21 Configurations and the von Mises stress of the satellite and solar-array system at some time steps (Color figure online)

the adjacent solar panels is $\theta_0 = 2^\circ$, as shown in Fig. 20(b). Considering the contact of solar panels and the contact between solar panel and satellite, it requires the STS and STRS contact elements. The normal and tangential penalty parameters for the STS and STRS contact elements are $\epsilon_N = \epsilon_T = 10^5 \text{ N/m}^3$, and the static and dynamic frictional coefficients are $\mu_s = \mu_d = 0.3$. In addition, the points D and D_1 are subjected to a prescribed translational displacement vector $\mathbf{d}(t) = [d(t) \ 0 \ 0]^T \text{ m}$. The piecewise function is

$$d(t) = \begin{cases} 0.5a_d t^2 + s_0, & 0 \leq t < t_1, \\ 0.5a_d t_1^2 + a_d t_1(t - t_1) + s_0, & t_1 \leq t < t_2, \\ L^P - 0.5a_d(t_3 - t)^2, & t_2 \leq t < t_3, \\ L^P, & t_3 \leq t \leq t_e, \end{cases} \quad (55)$$

where $t_1 = 12 \text{ s}$, $t_2 = 108 \text{ s}$, $t_3 = 120 \text{ s}$ and $t_e = 200 \text{ s}$. $s_0 = 0.25L^P \cos(\theta_0/2)$ is the initial x coordinate, and $a_d = (L^P - s_0)/t_1 t_2$ ensures that the deployment of the solar array ends with a fully deployed configuration, and the maximum velocity of the drive is defined as $v_m = v_c = a_d t_1$.

Based on the complete rigid–flexible–thermal coupling model proposed in this paper, the changes of configuration at some time steps are shown in Fig. 21, and the color maps represent the distribution of the von Mises stress. The initial stress of the folded solar panels is set to zero, and then the solar panels are gradually deployed applied with the driving constraints. Due to contact, it can be found that the stresses of panels 1 and 2 are greater than those of panels 3 and 4 at $t = 30 \text{ s}$ and $t = 60 \text{ s}$. As the thermal loads continue, panels 3 and 4 experience greater thermal stress, which can be seen in the configurations at $t = 90 \text{ s}$ and $t = 120 \text{ s}$. After the solar array is fully deployed, we can observe that the stress distribution of the four solar panels is relatively balanced, accompanied by obvious thermal deflection.

Figure 22 presents the time history of temperature gradients of the points P , B , and Q during the deployment of the solar array, and these test points can comprehensively reflect the heating conditions of the solar array. It can be seen that for $t < 50 \text{ s}$, the temperature gradient at point P has a zero value, which is due to the fact that point P is in the shadow region at the time of contact and cannot receive solar radiation. Since one of the plates connecting the point B is in the shadow region at the initial stage, the temperature gradient rate at point B is lower than that at point Q . This why panels 1 and 2 experience greater thermal stress than panels 3 and 4 during the deployment of the solar array. Finally, the solar panels are fully deployed, and the temperature gradients of the three points are the same.

Fig. 22 Time history of temperature gradients of points *P*, *B*, and *Q* (see Fig. 20) in the *z* direction (Color figure online)

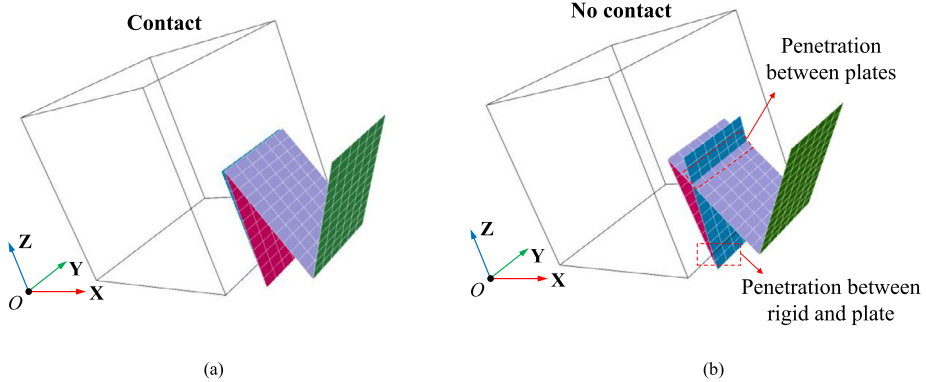
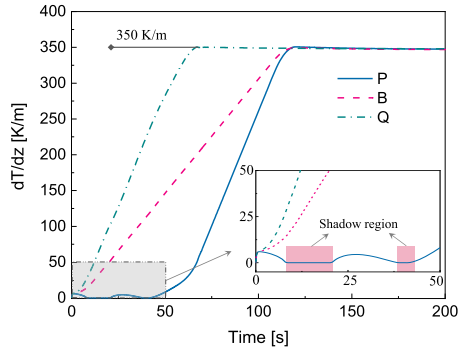


Fig. 23 Configurations of the (a) contact model; (b) no contact model at $t = 30$ s (Color figure online)

Therefore, the influence of contact and thermal loads on the deployment process of the solar array is essential, which needs to be paid more attention to in engineering.

7.2.1 Influence of contact

In order to illustrate the necessity of contact, two models are employed. The first one considers the integration of the STS and STRS contact elements, and the other does not consider contact. For the sake of intuitiveness, the configuration of the satellite and solar-array system at $t = 30$ s is selected for analysis, as shown in Fig. 23. It can be seen in Fig. 23(a) that the solar array can deploy properly without overpenetration in consideration of contact. On the contrary, it is clearly observed that the large penetration appears not only between the solar panels, but also between the satellite and the solar panels when the contact is not taken into account. In conclusion, for the deployment of the satellite and solar-array system, it requires a combination of STS and STRS contact elements to avoid mutual penetration, thereby ensuring computation accuracy.

With the view of further analyzing the effect of contact, Fig. 24 depicts the time history of coordinate *x* of points *B* and *P* obtained by the contact and no contact models. It can be seen that the values of the coordinate *x* of points *B* and *P* are less than 1, that is, the solar panels penetrate into the satellite, which violates the real situation. After the contact no longer occurs, the curves of the two contact models gradually tend to be consistent, and

Fig. 24 Time history of coordinates x of points B and P in different contact models (Color figure online)

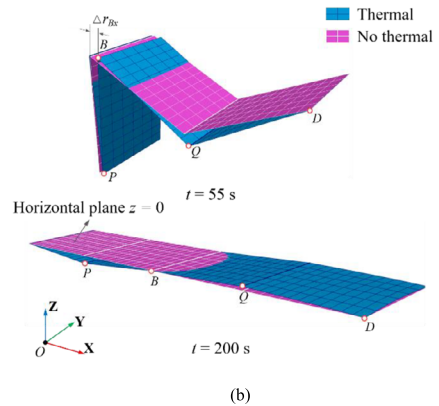
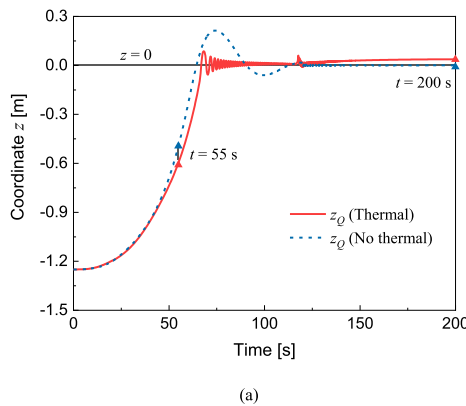
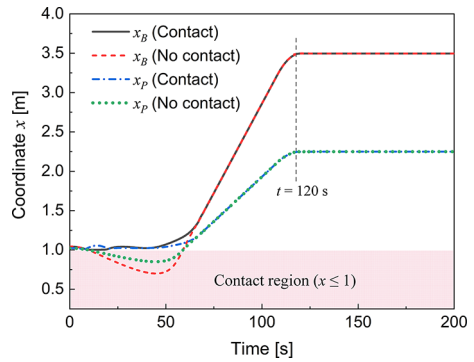


Fig. 25 (a) Time history of coordinates z of point Q in different thermal models; (b) Configurations of different thermal models at $t = 55$ s and $t = 200$ s (Color figure online)

the solar array is fully deployed at $t = 120$ s. Therefore, we can conclude that the contact affects not only the motions of the system, but also the shadow regions, which is related to the intensity of the solar radiation.

7.2.2 Influence of thermal load

Since the thermal loads have a significant effect on the deployment of the solar array, two different thermal models are compared and analyzed in this section. Figure 25(a) presents the time history of coordinates z of point Q obtained by the thermal and no thermal models, respectively. By observing the coordinates z_Q of the two models, it can be seen that when the solar panels 3 and 4 are fully deployed, the thermal model excites high-frequency oscillations with gradually decreasing amplitudes. Combined with the configuration at $t = 55$ s in Fig. 25(b), it can be seen that since point B of the no thermal model moves later than that of the thermal model, point Q has a greater vertical velocity as it passes the horizontal position, resulting in a greater offset magnitude. In addition, the final configurations of the thermal and no thermal models at $t = 200$ s are also presented in Fig. 25(b), in which we can observe that obvious deflections of the thermal model occur at points P and Q due to the effects of the boundary constraints and the thermal loads, which cannot be obtained by the no thermal model.

Fig. 26 Time history of deflection of point P in different thermal models (Color figure online)

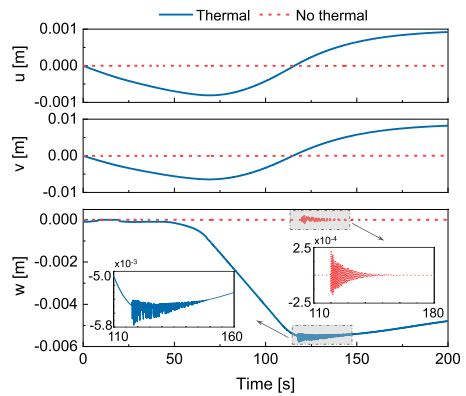
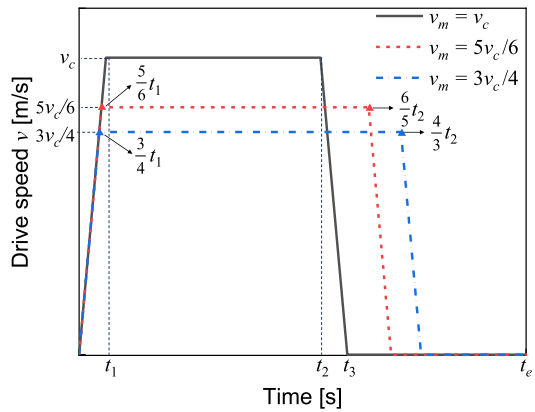


Fig. 27 Drive-speed curves in three cases (Color figure online)



To further analyze the thermal expansion and deflection, the time history of the deflection of point P in different models is given in Fig. 26. Here, u , v , and w denote the deflection of point P in the x , y , and z directions, respectively. The values of u and v remain zero in the no thermal model, but eventually exhibit positive expansion in the thermal model. By comparing the curve of w in the two models, it can be observed that when the solar array is fully deployed at $t = 120$ s, the vibration amplitude of the thermal model is greater than that of the no thermal model, and the decay time is longer. From the results in the figure, it is necessary to pay attention to the phenomenon of thermal deflection during the deployment of the solar array.

7.2.3 Comparison of different drive speeds

In engineering, the effect of drive speed on the satellite and solar-array system is another issue of concern. In this section, we focus on comparing the results of three different drive speeds acting on the solar array in a thermal environment. As illustrated in Fig. 20, the points D and D_1 are subjected to a prescribed translational displacement along the x direction. As shown in Fig. 27, the drive-speed curves in different cases have the same displacement at $t = t_e$, in which the black curve represents the basic model, and its expression refers to Eq. (55).

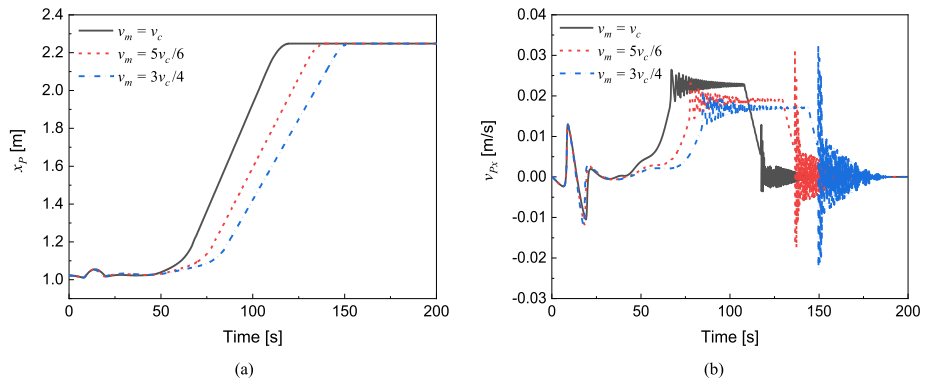


Fig. 28 Time histories of (a) displacement; (b) velocity of point P in the x direction in different cases (Color figure online)

Figure 28 plots the dynamic response of point P at three different drive speeds. It can be seen in Fig. 28(a) that the deployment times of the solar array in the three cases are significantly different, and the changes of x_P are relatively stable. From the results in Fig. 28(b), we can observe that there are two obvious high-frequency vibrations during the deployment of the solar array. The first occurs when the solar panels 3 and 4 are fully deployed, another occurs when the solar panels 1 and 2 are fully deployed. Since the thermal effect is positively related to the action time of the thermal load, the thermal stress increases with decreasing drive speed, resulting in a greater amplitude of oscillation, especially when the plates are fully deployed.

8 Conclusions

A strong rigid–flexible–thermal coupling dynamic model for a hub and multiplate multi-body system with large deformations and frictional contact interactions is proposed. An ANCF thin-plate element with thermoelasticity is developed, and the temperature field is expressed with Taylor polynomials to gain the heat conduction equations. Accounting for the influences of the attitude motion and structural deformation on the intensity of the solar radiation, a complete rigid–flexible–thermal coupling model is created. Subsequently, the STS and STRS frictional contact elements are developed, which can effectively avoid the mutual overpenetration and capture the stick–slip behavior. Furthermore, a new numerical approach combining the generalized- α method and a modified central-difference method is proposed to solve the strong rigid–flexible–thermal coupling equations, which improves the accuracy of the full coupled simulation by solving the heat-conduction equations and the dynamic equations simultaneously.

By setting comparative tests in ABAQUS, the correctness of the proposed thermal–structural coupling model is validated, and the necessity of the geometric nonlinearity is proved. Moreover, the advantages of the proposed model in capturing thermally induced vibration are revealed. To further demonstrate the effectiveness of the proposed rigid–flexible–thermal coupling method, two numerical simulations of the satellite and solar-array multibody system in a thermal environment are conducted. The first example compares the results of three dynamic models: RFTC model, RFCT model, and RFC model. Due to the consideration of the elastic deformation as well as the rigid-body motion on the intensity of

heat flux, RFTC model can reveal the phenomena of the thermally induced vibrations, which cannot be achieved by the other two models. Parameter analysis illustrates that the thermally induced vibration effect can be reduced through the decrease of the solar angle and the specific heat or the increase of the damping coefficient. Then, the nonlinear coupling behavior of the maneuvering satellite and solar-array system can be revealed by the proposed RFTC model. The second example is employed to analyze the deployment dynamic performance of the solar array in a thermal environment with frictional contact. It is concluded that the contact affects not only the motions of the system, but also the intensity of the solar radiation because of the shadow regions. Due to the effects of the boundary constraints and the thermal loads, obvious thermal deflection and high-frequency vibration can be induced, especially when the plates are fully deployed. Since the thermal effect is positively related to the action time of the thermal load, the amplitude of thermal vibration increases with the decreasing of the drive speed.

Appendix. Solution scheme for the rigid–flexible–thermal coupling equations

The solution scheme for the rigid–flexible–thermal coupling equations is divided into the following three steps:

- *Step1: Prediction of the initial value*

Assuming that $\ddot{\mathbf{q}}_d^{t+\Delta t} = \mathbf{0}$, we combine Taylor’s formula, the generalized- α method, and a modified central-difference method to predict $\mathbf{a}_d^{t+\Delta t}$, $\mathbf{q}_d^{t+\Delta t}$, $\dot{\mathbf{q}}_d^{t+\Delta t}$, $\boldsymbol{\lambda}^{t+\Delta t}$, $\mathbf{p}^{t+\Delta t}$, as follows:

$$\mathbf{a}_d^{t+\Delta t} = \frac{\alpha_f}{1 - \alpha_m} \ddot{\mathbf{q}}_d^t - \frac{\alpha_m}{1 - \alpha_m} \mathbf{a}_d^t, \tag{56}$$

$$\mathbf{q}_d^{t+\Delta t} = \mathbf{q}_d^t + \Delta t \dot{\mathbf{q}}_d^t + \Delta t^2 (0.5 - \beta) \mathbf{a}_d^t + \Delta t^2 \beta \mathbf{a}_d^{t+\Delta t}, \tag{57}$$

$$\dot{\mathbf{q}}_d^{t+\Delta t} = \dot{\mathbf{q}}_d^t + \Delta t (1 - \gamma) \mathbf{a}_d^t + \Delta t \gamma \mathbf{a}_d^{t+\Delta t}, \tag{58}$$

$$\boldsymbol{\lambda}^{t+\Delta t} = \boldsymbol{\lambda}^t, \tag{59}$$

$$\mathbf{p}^{t+\Delta t} = \theta \mathbf{p}^{t+\Delta t} + (1 - \theta) \mathbf{p}^t, \tag{60}$$

where

$$\alpha_m = \frac{2\rho_\infty - 1}{\rho_\infty + 1}, \quad \alpha_f = \frac{\rho_\infty}{\rho_\infty + 1}, \tag{61}$$

$$\gamma = 0.5 + \alpha_f - \alpha_m, \quad \beta = 0.25 (\gamma + 0.5)^2, \tag{62}$$

and the numerical parameters $\rho_\infty, \theta \in [0, 1]$. The numerical parameters in this paper are taken as $\rho_\infty = 0.6, \theta = 0.5$.

- *Step2: Transformation into nonlinear algebraic equations*

The dynamic equations can be transformed into nonlinear algebraic equations using the generalized- α method [53]

$$\left[\begin{array}{c} \mathbf{M}_d \ddot{\mathbf{q}}_d^{t+\Delta t} + \mathbf{C}_d \dot{\mathbf{q}}_d^{t+\Delta t} + \Phi_{\mathbf{q}_d}^T(\mathbf{q}_d^{t+\Delta t}) \boldsymbol{\lambda}^{t+\Delta t} - \mathbf{Q}_d(\mathbf{q}_d^{t+\Delta t}, \mathbf{p}^{t+\Delta t}) \\ \Phi(\mathbf{q}_d^{t+\Delta t}, t + \Delta t) \end{array} \right] = \mathbf{0}, \tag{63}$$

where

$$\frac{\partial \ddot{\mathbf{q}}_d^{t+\Delta t}}{\mathbf{q}_d^{t+\Delta t}} = \beta' \mathbf{I}, \quad \frac{\partial \dot{\mathbf{q}}_d^{t+\Delta t}}{\mathbf{q}_d^{t+\Delta t}} = \gamma' \mathbf{I}, \tag{64}$$

$$\beta' = \frac{1 - \alpha_m}{(1 - \alpha_f) \beta \Delta t^2}, \quad \gamma' = \frac{\gamma}{\beta \Delta t}. \tag{65}$$

The heat-conduction equations in Eq. (48) are transformed into nonlinear algebraic equations by a modified central-difference method [49]

$$\bar{\mathbf{K}} \mathbf{p}^{t+\Delta t} - \bar{\mathbf{Q}}(\mathbf{q}_d^{t+\Delta t}, \mathbf{p}^{t+\Delta t}) = \mathbf{0}, \tag{66}$$

where

$$\bar{\mathbf{K}} = \frac{\mathbf{M}_T}{\Delta t} + \theta \mathbf{K}_T, \tag{67}$$

$$\bar{\mathbf{Q}} = \left[\frac{\mathbf{M}_T}{\Delta t} - (1 - \theta) \mathbf{K}_T \right] \mathbf{p}^t + (1 - \theta) \mathbf{F}_T^t + \theta \mathbf{F}_T^{t+\Delta t}. \tag{68}$$

• *Step3: Solution of the combined nonlinear algebraic equations*

According to Eqs. (A8) and (A11), the combined nonlinear algebraic equations are rewritten as

$$\begin{aligned} &\Psi(\mathbf{q}_d^{t+\Delta t}, \mathbf{p}^{t+\Delta t}, \boldsymbol{\lambda}^{t+\Delta t}, t + \Delta t) \\ &= \begin{bmatrix} \mathbf{M}_d \ddot{\mathbf{q}}_d^{t+\Delta t} + \mathbf{C}_d \dot{\mathbf{q}}_d^{t+\Delta t} + \Phi_{\mathbf{q}_d}^T(\mathbf{q}_d^{t+\Delta t}) \boldsymbol{\lambda}^{t+\Delta t} - \mathbf{Q}_d(\mathbf{q}_d^{t+\Delta t}, \mathbf{p}^{t+\Delta t}) \\ \Phi_{\mathbf{q}_d}(\mathbf{q}_d^{t+\Delta t}, t + \Delta t) \\ \bar{\mathbf{K}} \mathbf{p}^{t+\Delta t} - \bar{\mathbf{Q}}(\mathbf{q}_d^{t+\Delta t}, \mathbf{p}^{t+\Delta t}) \end{bmatrix} = \mathbf{0}. \end{aligned} \tag{69}$$

The Newton–Raphson algorithm is used to find a solution of Eq. (A14). At an iteration step k , the following equation is solved for a correction $\Delta \mathbf{q}_{(k)}^{t+\Delta t}$:

$$\Delta \mathbf{q}_{(k)}^{t+\Delta t} = \begin{bmatrix} \Delta \mathbf{p}_{(k)}^{t+\Delta t} \\ \Delta \mathbf{q}_{d(k)}^{t+\Delta t} \\ \Delta \boldsymbol{\lambda}_{(k)}^{t+\Delta t} \end{bmatrix} = - \begin{bmatrix} \frac{\partial \Psi}{\partial \mathbf{p}^{t+\Delta t}} & \frac{\partial \Psi}{\partial \mathbf{q}_d^{t+\Delta t}} & \frac{\partial \Psi}{\partial \boldsymbol{\lambda}^{t+\Delta t}} \end{bmatrix}^{-1} \Psi, \tag{70}$$

where

$$\frac{\partial \Psi}{\partial \mathbf{p}^{t+\Delta t}} = \begin{bmatrix} -\frac{\partial \mathbf{Q}_d(\mathbf{q}_{d(k)}^{t+\Delta t}, \mathbf{p}_{(k)}^{t+\Delta t})}{\partial \mathbf{p}^{t+\Delta t}} \\ \mathbf{0} \\ \bar{\mathbf{K}} - \frac{\partial \bar{\mathbf{Q}}(\mathbf{q}_{d(k)}^{t+\Delta t}, \mathbf{p}_{(k)}^{t+\Delta t})}{\partial \mathbf{p}^{t+\Delta t}} \end{bmatrix}, \tag{71}$$

$$\frac{\partial \Psi}{\partial \mathbf{q}_d^{t+\Delta t}} = \begin{bmatrix} \alpha' \mathbf{M}_d + \beta' \mathbf{C}_d + \frac{\partial (\Phi_{\mathbf{q}_d}^T(\mathbf{q}_{d(k)}^{t+\Delta t}) \boldsymbol{\lambda}_{(k)}^{t+\Delta t})}{\partial \mathbf{q}_d^{t+\Delta t}} - \frac{\partial (\mathbf{Q}_d(\mathbf{q}_{d(k)}^{t+\Delta t}, \mathbf{p}_{(k)}^{t+\Delta t}))}{\partial \mathbf{q}_d^{t+\Delta t}} \\ \Phi_{\mathbf{q}_d}(\mathbf{q}_{d(k)}^{t+\Delta t}) \\ -\frac{\partial \bar{\mathbf{Q}}(\mathbf{q}_{d(k)}^{t+\Delta t}, \mathbf{p}_{(k)}^{t+\Delta t})}{\partial \mathbf{q}_d^{t+\Delta t}} \end{bmatrix}, \tag{72}$$

$$\frac{\partial \Psi}{\partial \lambda^{t+\Delta t}} = \begin{bmatrix} \Phi_{\mathbf{q}_d}^T (\mathbf{q}_d^{t+\Delta t}) \\ \mathbf{0} \\ \mathbf{0} \end{bmatrix}. \quad (73)$$

An improved estimate can be obtained as

$$\mathbf{q}_{(k+1)}^{t+\Delta t} = \mathbf{q}_{(k)}^{t+\Delta t} + \Delta \mathbf{q}_{(k)}^{t+\Delta t}, \quad k = 0, 1, \dots, \quad (74)$$

until the precision condition $\|\Delta \mathbf{q}_{(k)}^{t+\Delta t}\| \leq \delta$ is satisfied, in which δ is the precision error.

Author contributions Tingting Yuan proposed the conceptualization and methodology of this study, and performed simulation and analysis, and wrote the main manuscript text. Bo Lei performed the validation and the data analysis. Jinyang Liu helped perform the formulations and analysis with constructive discussion. Yunli Wu helped perform simulation. All authors reviewed the manuscript.

Funding This research was supported by the General Program (No. 12272221) of the National Natural Science Foundation of China, the Key Program (No. 11932001) of the National Natural Science Foundation of China, and the International (Regional) Cooperation and Exchange Programs (No. 12311530038) of the National Natural Science Foundation of China, for which the authors are grateful. This research was also supported by the Key Laboratory of Hydrodynamics (Ministry of Education).

Declarations

Competing interests The authors declare no competing interests.

References

- Thornton, E.A., Kim, Y.A.: Thermally induced bending vibrations of a flexible rolled-up solar array. *J. Spacecr. Rockets* **30**(4), 438–448 (1993)
- Johnston, J.D., Thornton, E.A.: Thermally induced attitude dynamics of a spacecraft with a flexible appendage. *J. Guid. Control Dyn.* **21**(4), 581–587 (1998)
- Johnston, J.D., Thornton, E.A.: Thermally induced dynamics of satellite solar panels. *J. Spacecr. Rockets* **37**(5), 604–613 (2000)
- Fan, W., Liu, J.: Geometric nonlinear formulation for thermal-rigid-flexible coupling system. *Acta Mech. Sin.* **29**(5), 728–737 (2013)
- Shen, Z., Tian, Q., Liu, X., Hu, G.: Thermally induced vibrations of flexible beams using absolute nodal coordinate formulation. *Aerosp. Sci. Technol.* **29**(1), 386–393 (2013)
- Shen, Z., Hu, G.: Thermally induced dynamics of a spinning spacecraft with an axial flexible boom. *J. Spacecr. Rockets* **52**, 1503–1508 (2015)
- Shen, Z., Hu, G.: Thermoelastic–structural analysis of space thin-walled beam under solar flux. *AIAA J.* **57**(4), 1781–1785 (2019)
- Čepon, G., Starc, B., Zupančič, B., Boltežar, M.: Coupled thermo-structural analysis of a bimetallic strip using the absolute nodal coordinate formulation. *Multibody Syst. Dyn.* **41**(4), 391–402 (2017)
- Liu, L., Sun, S., Cao, D., Liu, X.: Thermal-structural analysis for flexible spacecraft with single or double solar panels: a comparison study. *Acta Astronaut.* **154**, 33–43 (2019)
- Liu, L., Cao, D., Huang, H., Shao, C., Xu, Y.: Thermal-structural analysis for an attitude maneuvering flexible spacecraft under solar radiation. *Int. J. Mech. Sci.* **126**, 161–170 (2017)
- Liu, L., Wang, X., Sun, S., Cao, D., Liu, X.: Dynamic characteristics of flexible spacecraft with double solar panels subjected to solar radiation. *Int. J. Mech. Sci.* **151**, 22–32 (2019)
- Li, Y., Wang, C., Huang, W.: Rigid–flexible–thermal analysis of planar composite solar array with clearance joint considering torsional spring, latch mechanism and attitude controller. *Nonlinear Dyn.* **96**(3), 2031–2053 (2019)
- Liu, J., Pan, K.: Rigid–flexible–thermal coupling dynamic formulation for satellite and plate multibody system. *Aerosp. Sci. Technol.* **52**, 102–114 (2016)
- Shabana, A.A.: Flexible multibody dynamics: review of past and recent developments. *Multibody Syst. Dyn.* **1**(2), 189–222 (1997)

15. Dmitrochenko, O.N., Pogorelov, D.Y.: Generalization of plate finite elements for absolute nodal coordinate formulation. *Multibody Syst. Dyn.* **10**(1), 17–43 (2003)
16. Dmitrochenko, O., Mikkola, A.: Two simple triangular plate elements based on the absolute nodal coordinate formulation. *J. Comput. Nonlinear Dyn.* **3**(4), 041012 (2008)
17. Dufva, K., Shabana, A.A.: Analysis of thin plate structures using the absolute nodal coordinate formulation. *Proc. Inst. Mech. Eng., Part K, J. Multi-Body Dyn.* **219**(4), 345–355 (2005)
18. Ren, H.: Fast and robust full-quadrature triangular elements for thin plates/shells with large deformations and large rotations. *J. Comput. Nonlinear Dyn.* **10**(5), 051018 (2015)
19. Schwab, A.L., Gerstmayr, J., Meijaard, J.P.: Comparison of three-dimensional flexible thin plate elements for multibody dynamic analysis: finite element formulation and absolute nodal coordinate formulation. In: *ASME 2007 International Design Engineering Technical Conferences and Computers and Information in Engineering Conference*, Las Vegas, Nevada, USA (2007)
20. Vaziri Sereshk, M., Salimi, M.: Comparison of finite element method based on nodal displacement and absolute nodal coordinate formulation (ANCF) in thin shell analysis. *Int. J. Numer. Methods Biomed. Eng.* **27**(8), 1185–1198 (2011)
21. Hyldahl, P., Mikkola, A.M., Balling, O., Sopanen, J.T.: Behavior of thin rectangular ANCF shell elements in various mesh configurations. *Nonlinear Dyn.* **78**(2), 1277–1291 (2014)
22. Liu, C., Tian, Q., Hu, H.: New spatial curved beam and cylindrical shell elements of gradient-deficient absolute nodal coordinate formulation. *Nonlinear Dyn.* **70**(3), 1903–1918 (2012)
23. Gerstmayr, J., Sugiyama, H., Mikkola, A.: Review on the absolute nodal coordinate formulation for large deformation analysis of multibody systems. *J. Comput. Nonlinear Dyn.* **8**(3), 031016 (2013)
24. Liu, C., Tian, Q., Yan, D., Hu, H.: Dynamic analysis of membrane systems undergoing overall motions, large deformations and wrinkles via thin shell elements of ANCF. *Comput. Methods Appl. Mech. Eng.* **258**, 81–95 (2013)
25. Shen, Z., Hu, G.: Thermally induced vibrations of solar panel and their coupling with satellite. *Int. J. Appl. Mech.* **5**, 1350031 (2013)
26. Cui, Y., Yu, Z., Lan, P.: A novel method of thermo-mechanical coupled analysis based on the unified description. *Mech. Mach. Theory* **134**, 376–392 (2019)
27. Cui, Y., Lan, P., Zhou, H., Yu, Z.: The rigid–flexible–thermal coupled analysis for spacecraft carrying large-aperture paraboloid antenna. *J. Comput. Nonlinear Dyn.* **15**(3), 031003 (2020)
28. Wriggers, P.: *Computational Contact Mechanics*. Springer, Berlin (2006)
29. Konyukhov, A., Izi, R.: *Introduction to Computational Contact Mechanics: A Geometrical Approach*. Wiley, Chichester (2015)
30. Flores, P.: Contact mechanics for dynamical systems: a comprehensive review. *Multibody Syst. Dyn.* **54**(2), 127–177 (2022)
31. Flores, P.: Contact mechanics for dynamical systems: a comprehensive review. *Multibody Syst. Dyn.* **54**(2), 127–177 (2022). <https://doi.org/10.1007/s11044-021-09803-y>
32. Konyukhov, A., Schweizerhof, K.: *Computational Contact Mechanics: Geometrically Exact Theory for Arbitrary Shaped Bodies*. Springer, Berlin (2013)
33. Schweizerhof, K., Konyukhov, A.: Covariant description for frictional contact problems. *Comput. Mech.* **35**, 190–213 (2005)
34. Yu, L., Zhao, Z., Tang, J., Ren, G.: Integration of absolute nodal elements into multibody system. *Nonlinear Dyn.* **62**(4), 931–943 (2010)
35. Shi, J., Liu, Z., Hong, J.: Dynamic contact model of shell for multibody system applications. *Multibody Syst. Dyn.* **44**(4), 335–366 (2018)
36. Sun, D., Liu, C., Hu, H.: Dynamic computation of 2D segment-to-segment frictionless contact for a flexible multibody system subject to large deformation. *Mech. Mach. Theory* **140**, 350–376 (2019)
37. Sun, D., Liu, C., Hu, H.: Dynamic computation of 2D segment-to-segment frictional contact for a flexible multibody system subject to large deformations. *Mech. Mach. Theory* **158**, 104197 (2021)
38. Gay Neto, A., Wriggers, P.: Master-master frictional contact and applications for beam-shell interaction. *Comput. Mech.* **66**(6), 1213–1235 (2020)
39. Tang, L., Liu, J.: Frictional contact analysis of sliding joints with clearances between flexible beams and rigid holes in flexible multibody systems. *Multibody Syst. Dyn.* **49**(2), 155–179 (2019)
40. Lei, B., Ma, Z., Liu, J., Liu, C.: Dynamic modelling and analysis for a flexible brush sampling mechanism. *Multibody Syst. Dyn.* **56**(4), 335–365 (2022)
41. Yuan, T., Liu, Z., Zhou, Y., Liu, J.: Dynamic modeling for foldable origami space membrane structure with contact-impact during deployment. *Multibody Syst. Dyn.* **50**(1), 1–24 (2020)
42. Yuan, T., Tang, L., Liu, Z., Liu, J.: Nonlinear dynamic formulation for flexible origami-based deployable structures considering self-contact and friction. *Nonlinear Dyn.* **106**(3), 1789–1822 (2021)
43. Boley, B., Weiner, J.: *Theory of Thermal Stresses*. Dover Civil and Mechanical Engineering Series. Dover, New York (1960)

44. Hetnarski, R.B.M.: Thermal Stresses – Advanced Theory and Applications. Solid Mechanics and Its Applications. Springer, Dordrecht (2008)
45. Eslami, M., Hetnarski, R., Ignaczak, J., Noda, N., Sumi, N., Tanigawa, Y.: Theory of Elasticity and Thermal Stresses: Explanations, Problems and Solutions. Springer, Dordrecht (2013)
46. Liu, J., Lu, H.: Thermal effect on the deformation of a flexible beam with large kinematical driven overall motions. *Eur. J. Mech. A, Solids* **26**(1), 137–151 (2007)
47. Yuan, T., Tang, L., Liu, J.: Dynamic modeling and analysis for inflatable mechanisms considering adhesion and rolling frictional contact. *Mech. Mach. Theory* **184**, 105295 (2023)
48. Tang, L., Liu, J.: Modeling and analysis of sliding joints with clearances in flexible multibody systems. *Nonlinear Dyn.* **94**(4), 2423–2440 (2018)
49. Wang, X.: Finite Element Method. Tsinghua University Press, Beijing (2003)
50. Haug, E.J.: Computer Aided Kinematics and Dynamics of Mechanical Systems. Allyn & Bacon, Boston (1989)
51. Hong, J.: Computational Dynamics of Multibody Systems. Higher Education Press, Beijing (1999)
52. Liu, Z., Liu, J.: Experimental validation of rigid-flexible coupling dynamic formulation for hub–beam system. *Multibody Syst. Dyn.* **40**(3), 303–326 (2017)
53. Arnold, M., Brüls, O.: Convergence of the generalized- α scheme for constrained mechanical systems. *Multibody Syst. Dyn.* **18**(2), 185–202 (2007)
54. Köbis, M., Arnold, M.: Convergence of generalized- α time integration for nonlinear systems with stiff potential forces. *Multibody Syst. Dyn.* **37**(1), 107–125 (2016)
55. Noels, L., Stainier, L., Ponthot, J.P.: Self-adapting time integration management in crash-worthiness and sheet metal forming computations. *Int. J. Veh. Des.* **30**(1–2), 67–114 (2002)

Publisher's Note Springer Nature remains neutral with regard to jurisdictional claims in published maps and institutional affiliations.

Springer Nature or its licensor (e.g. a society or other partner) holds exclusive rights to this article under a publishing agreement with the author(s) or other rightsholder(s); author self-archiving of the accepted manuscript version of this article is solely governed by the terms of such publishing agreement and applicable law.